JCTC Journal of Chemical Theory and Computation

ARTICLE

pubs.acs.org/JCTC

Understanding RNA Flexibility Using Explicit Solvent Simulations: The Ribosomal and Group I Intron Reverse Kink-Turn Motifs

Petr Sklenovský,[†] Petra Florová,[†] Pavel Banáš,[†] Kamila Réblová,[‡] Filip Lankaš,[§] Michal Otyepka,[*,†] and Jiří Šponer[*,‡]

[†]Regional Centre of Advanced Technologies and Materials, Department of Physical Chemistry, Faculty of Science, Palacky University Olomouc, tr. 17. listopadu 12, 771 46 Olomouc, Czech Republic

[‡]Institute of Biophysics, Academy of Sciences of the Czech Republic, Kralovopolska 135, 612 65 Brno, Czech Republic

[§]Centre for Complex Molecular Systems and Biomolecules, Institute of Organic Chemistry and Biochemistry, Flemingovo nam. 2, 166 10 Praha 6, Czech Republic

Supporting Information

ABSTRACT: Reverse kink-turn is a recurrent elbow-like RNA building block occurring in the ribosome and in the group I intron. Its sequence signature almost matches that of the conventional kink-turn. However, the reverse and conventional kink-turns have opposite directions of bending. The reverse kink-turn lacks basically any tertiary interaction between its stems. We report unrestrained, explicit solvent molecular dynamics simulations of ribosomal and intron reverse kink-turns (54 simulations with 7.4 μs of data in total) with different variants (*ff*94, *ff*99, *ff*99bsc0, *ff*99χ_{OL}, and *ff*99bsc0χ_{OL}) of the Cornell et al. force field. We test several ion conditions and two water models. The simulations characterize the directional intrinsic flexibility of reverse kink-turns pertinent to their folded functional geometries. The reverse kink-turns are the most flexible RNA motifs studied so far by explicit solvent simulations which are capable at the present simulation time scale to spontaneously and reversibly sample a wide range of geometries from tightly kinked ones through flexible intermediates up to extended, unkinked structures. A possible biochemical role of the flexibility is discussed. Among the tested force fields, the latest χ_{OL} variant is essential to obtaining stable trajectories while all force field versions lacking the χ correction are prone to a swift degradation toward senseless ladder-like structures of stems, characterized by high-*anti* glycosidic torsions. The type of explicit water model affects the simulations considerably more than concentration and the type of ions.

INTRODUCTION

Kink-turn (K-turn) is a recurrent RNA structural motif occurring in the ribosome,[1−3] mRNA,[4,5] riboswitches,[6,7] snoRNAs,[8] and the human U4 snRNA.[9,10] K-turn plays an important role in RNA structure; for instance, it is involved in ribosome intersubunit bridges[11] and specific binding of ribosomal proteins.[12] Some K-turns are also localized in flexible segments of the ribosome which play a prominent role in the elongation. The X-ray data identified the K-turn motif as a well structured 3D RNA building block mediating a sharp bend (∼120°) of phosphodiester backbone between consecutive RNA helices. Solution experiments conducted for isolated K-turns suggested that free in solution K-turn possesses two (kinked and open) states which are in a dynamic equilibrium. The ratio of kinked/open states depends on the concentration of metal ions. At a high concentration of divalent metal ions, K-turn prefers the kinked conformation, while at low concentrations, K-turn favors the open geometry.[13−15] Besides metal ions, proteins are also able to stabilize the kinked structures.[12,16] Molecular dynamics (MD) simulations of free K-turns in their folded (kinked) topology show that K-turns are anisotropic and nonharmonic flexible structures displaying hinge-like dynamics around the folded geometry on a fast nanosecond time scale.[17−22]

Considering structural features of K-turn, a single-stranded internal bulge of K-turn forms a sharp kink between the helical axes of two consecutive RNA helices. The bulge usually contains three nucleotides, while the middle base is unstacked and flipped out. The RNA helix at the 5′ site of the bulge is a canonical stem (C-stem) consisting of Watson−Crick (WC) C═G base pairs. The second helix at the 3′ site of the bulge is a noncanonical stem (NC-stem) with two or three tandem *trans*-Hoogsteen/sugar-edge (*t*HS) A/G base pairs flanking the bulge.[23,24] Two of these *t*HS A/G base pairs neighboring the bulge are highly conserved. The structure of K-turn is stabilized by two tertiary interactions involving these two conserved *t*HS A/G base pairs of the NC-stem (see, e.g., Figure 1 in ref 16 for the annotation of the K-turn structure). The first tertiary interaction is *trans*-sugar-edge/sugar-edge (*t*SS) base pair comprising a hydrogen bond (H-bond) between the 2′-OH hydroxyl group of the 5′-most nucleotide of the bulge and N1 nitrogen of adenine of the *t*HS A/G base pair of the NC-stem adjacent to the 3′ site of the bulge. This interaction is essential for the folding of K-turns.[25,26] The second tertiary interaction is the A-minor interaction[27] between adenine of the second *t*HS A/G base pair in the NC-stem and the terminal base pair of the C-stem adjacent to the bulge. The A-minor interaction significantly contributes to the topology of K-turn and is essential for its internal structural dynamics.[20]

Received: March 24, 2011
Published: July 28, 2011

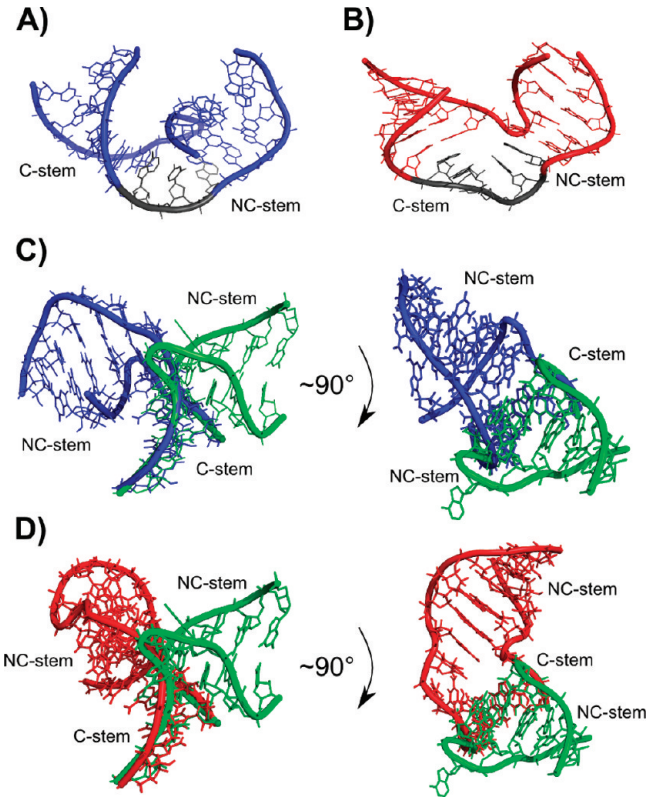

Figure 1. (A and B) The three-dimensional structures of the studied revKt-P9/9.0 (in blue) and revKt-54 (in red), respectively. Bulge regions are in gray. (C and D) The depiction of the opposite direction of revKt-P9/9.0 (blue) and revKt-54 (red) bends, respectively, in comparison to the nearly consensus ribosomal K-turn Kt-7 structure (green) from *H.m.* 23S rRNA. All systems are superimposed over their C-stems.

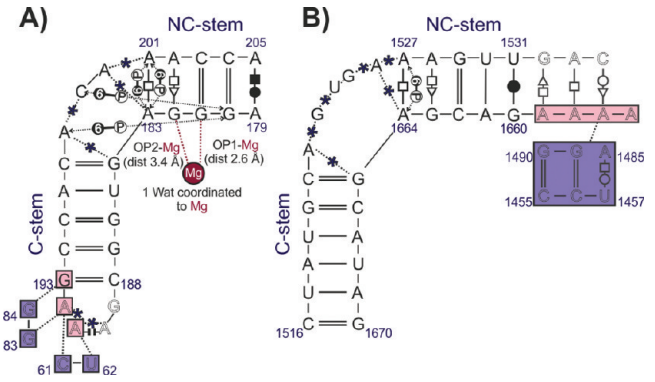

Figure 2. Secondary structures of revKt-P9/9.0 (A) and revKt-54 (B) annotated by standard classification[23,81] according to the X-ray structures (revKt-54, PDB 1S72; revKt-P9/9.0, PDB 1U6B). The dotted lines with stars in their centers highlight stacking interaction between the respective bases. Note that the coordination sphere of the Mg^{2+} is not complete in the X-ray structure due to resolution. Gray letters in panel A depict the GNRA tetraloop attached to the revKt-P9/9.0 C-stem (nucleotides 189−192; not included in MD simulations) and bases of the P5/5a intron segment (residues 61, 62, 83, and 84, not included in the simulations). In the pink squares of panel A are bases of the revKt-P9/9.0 C-stem and the GNRA tetraloop, which interact with bases of the P5/5a segment (highlighted in violet squares). Pink squares in panel B mark bases of revKt-54 NC-stem (four adenines), which interact with Helix 52 residues 1455−1457, 1485, and 1489−1490 (marked with violet rectangle). All bases colored in gray in panel B are not included in the simulations.

These two tertiary interactions bring together minor-groove sites of the two RNA stems.

The X-ray structure of the *Azoarcus* group I intron[28] revealed that the segment consisting of helices P9 and P9.0 (hereafter, revKt-P9/9.0) with almost the consensus K-turn sequence also adopts a bent conformation (the helices are mutually bent by ~90° in this particular case). The bending, however, goes in the opposite direction in comparison to the conventional K-turns (Figure 1A and C). It means that the major grooves of P9 and P9.0 stems are juxtaposed. Considering similarities to and differences from conventional K-turn (discussed below), the revKt-P9/9.0 motif is named as the reverse kink-turn (reverse K-turn). Similarly to the conventional K-turns, the bulge region is single-stranded and comprises three unpaired nucleotides: one helix is canonical (P9) containing mainly G═C WC base pairs, and the other is noncanonical (P9.0). In contrast to conventional K-turns that have a strictly conserved *t*HS A/G base pair in NC-stem adjacent to the bulge, revKt-P9/9.0 contains the *trans*-Hoogsteen/Hoogsteen (*t*HH) A201/A183 base pair at this position.[29] The second base pair of NC-stem is similar to the conventional K-turns *t*HS A202/G182 base pair (Figure 2A). The A201G mutant, having the K-turn consensual sequence, still retains the reverse K-turn fold in context of the intron structure.[29] This indicates that the fold is determined by external interactions (the overall context) rather than by local interactions and the primary sequence. Obviously, revKt-P9/9.0 lacks the A-minor interaction.[30] There is no flipped out base in the bulge between the stems, while all unpaired bases are stacked (Figure 2A). The base phosphate interactions between A198 and G180 and between C199 and G180 together with Mg^{2+} coordinated to G181 and G182 may stabilize the kinked conformation of revKt-P9/9.0 (Figure 2A).[31] There is a tertiary tetraloop−tetraloop receptor contact formed between the GNRA tetraloop adjacent to the revKt-P9/9.0 C-stem and bases of the intron P5/5a segment. The tetraloop−tetraloop receptor contact was suggested to be the leading factor in the bending of revKt-P9/9.0 toward the major groove.[29]

Another reverse K-turn was identified in the 23S rRNA of *Haloarcula marismortui* (*H.m.*).[31−33] This motif (hereafter, revKt-54) comprises helices 54 and 55 of 23S rRNA and bends again toward the major groove. The internal bulge, which bridges the helices, consists of five nucleotides, of which all are unpaired and stacked, and none is flipped out (Figures 1B,D and 2B). Helix 55 (NC-stem) contains *t*HH A1527/A1664 and *t*HS A1528/G1663 base pairs, being basically identical with the corresponding base pairs of the revKt-P9/9.0 NC-stem (cf. Figure 2A,B). Very recent automatic identification of RNA structural motifs using secondary structural alignment found another reverse K-turn motif comprising helices 55 and 56 of *H.m.* 23S rRNA.[34]

This study explores the intrinsic flexibility of two reverse K-turns (revKt-P9/9.0 and revKt-54) using an extensive set of conventional MD simulations in explicit solvent. We carried out altogether 54 simulations (typically on a 150 ns time scale) with a total simulation time of 7.4 μs (see Table 1 and Table S3, Supporting Information) under various conditions. Five variants of the Cornell et al. AMBER force field, several ionic conditions, and two explicit water models were considered. The basic purpose of this paper is two-fold. Besides characterizing the structural dynamics of reverse K-turns, we also investigate the performance and limitations of the simulation methods.

Table 1. List of MD Simulations[a]

simulated system (simulation label)[b]	water model + force field	ions	simulation length (ns)	time of "ladder like" transition (ns)[c]	RMSD (Å)[d]
revKt-P9/9.0 (INT-1)	TIP3P+*ff*99	19 Na^+, 1 Mg^{2+}	150	no transition	2.0 ± 0.6
revKt-P9/9.0 (INT-2)	TIP3P+*ff*99	19 Na^+, 1 Mg^{2+}	150	31	2.4 ± 0.6
revKt-P9/9.0 (INT-3)	SPC/E+*ff*99bsc0	40 K^+, 21 Cl^-, 1 Mg^{2+}	150	20	1.8 ± 0.3
revKt-P9/9.0 (INT-4)	SPC/E+*ff*99bsc0	40 K^+, 21 Cl^-, 1 Mg^{2+}	150	35	1.9 ± 0.3
revKt-P9/9.0 (INT-5)	TIP3P+*ff*99	21 Na^+	150	no transition	5.5 ± 1.0
revKt-P9/9.0 (INT-6)	TIP3P+*ff*99	21 Na^+	150	no transition	7.1 ± 1.5
revKt-P9/9.0 (INT-7)	TIP3P+*ff*99	21 Na^+	150	no transition	5.5 ± 2.3
revKt-P9/9.0 (INT-8)	TIP3P+*ff*99	21 Na^+	150	20	6.9 ± 1.5
revKt-P9/9.0 (INT-9)	TIP3P+*ff*99	21 Na^+	150	30	4.3 ± 1.5
revKt-P9/9.0 (INT-10)	TIP3P+*ff*99	21 Na^+	150	no transition	7.6 ± 1.5
revKt-P9/9.0 (INT-11)	SPC/E+*ff*99bsc0	42 K^+, 21 Cl^-	150	25	2.3 ± 0.8
revKt-P9/9.0 (INT-12)	SPC/E+*ff*99bsc0	42 K^+, 21 Cl^-	150	53	2.0 ± 0.6
revKt-P9/9.0 (INT-13)	SPC/E+*ff*99bsc0	42 K^+, 21 Cl^-	150	1.5	1.3 ± 0.3
revKt-P9/9.0 (INT-14)	SPC/E+*ff*99bsc0	42 K^+, 21 Cl^-	150	133	2.1 ± 0.7
revKt-P9/9.0 (INT-15)	SPC/E+*ff*99bsc0	42 K^+, 21 Cl^-	150	no transition	3.0 ± 1.1
revKt-P9/9.0 (INT-16)	SPC/E+*ff*99bsc0	42 K^+, 21 Cl^-	150	no transition	3.3 ± 1.2
revKt-P9/9.0 (INT-17)	TIP3P+*ff*94	21 Na^+	150	no transition	6.0 ± 1.9
revKt-P9/9.0 (INT-18)	TIP3P+*ff*94	19 Na^+, 1 Mg^{2+}	150	138	2.0 ± 0.6
revKt-P9/9.0 (INT-19)	TIP3P+*ff*99χ_{OL}	19 Na^+, 1 Mg^{2+}	150	no transition	4.8 ± 3.0
revKt-P9/9.0 (INT-20)	SPC/E+*ff*99bsc0χ_{OL}	40 K^+, 21 Cl^-, 1 Mg^{2+}	150	no transition	1.6 ± 0.3
revKt-P9/9.0 (INT-21)	TIP3P+*ff*99χ_{OL}	21 Na^+	150	no transition	7.7 ± 1.3
revKt-P9/9.0 (INT-22)	TIP3P+*ff*99χ_{OL}	21 Na^+	150	no transition	5.3 ± 2.4
revKt-P9/9.0 (INT-23)	TIP3P+*ff*99bsc0χ_{OL}	21 Na^+	150	no transition	5.7 ± 2.8
revKt-P9/9.0 (INT-24)	TIP3P+*ff*99bsc0χ_{OL}	21 Na^+	150	no transition	2.1 ± 0.8
revKt-P9/9.0 (INT-25)	SPC/E+*ff*99χ_{OL}	42 K^+, 21 Cl^-	150	no transition	2.3 ± 1.3
revKt-P9/9.0 (INT-26)	SPC/E+*ff*99bsc0χ_{OL}	42 K^+, 21 Cl^-	150	no transition	1.8 ± 0.5
revKt-54 (RIB-1)	TIP3P+*ff*94	25 Na^+	69	no transition	2.5 ± 0.9
revKt-54 (RIB-2)	TIP3P+*ff*94	12 Mg^{2+}, 1 Na^+	57	no transition	3.8 ± 0.7
revKt-54 (RIB-3)	TIP3P+*ff*99	25 Na^+	200	no transition	2.4 ± 0.7
revKt-54 (RIB-4)	TIP3P+*ff*99	25 Na^+	74	39	3.1 ± 0.8
revKt-54 (RIB-5)	TIP3P+*ff*99	12 Mg^{2+}, 1 Na^+	150	no transition	2.5 ± 0.7
revKt-54 (RIB-6)	TIP3P+*ff*99	12 Mg^{2+}, 1 Na^+	98	48	2.6 ± 0.7
revKt-54 (RIB-7)	TIP3P+*ff*99	23 Na^+	67	12	3.3 ± 0.9
revKt-54 (RIB-8)	TIP3P+*ff*99	23 Na^+	150	no transition	4.4 ± 0.8
revKt-54 (RIB-9)	SPC/E+*ff*99	46 K^+, 23 Cl^-	147	45	2.5 ± 0.7
revKt-54 (RIB-10)	SPC/E+*ff*99	46 K^+, 23 Cl^-	150	no transition	2.4 ± 0.5
revKt-54 (RIB-11)	TIP3P+*ff*99bsc0	23 Na^+	150	80	3.5 ± 1.0
revKt-54 (RIB-12)	TIP3P+*ff*99bsc0	23 Na^+	40	2	2.0 ± 0.5
revKt-54 (RIB-13)	SPC/E+*ff*99bsc0	46 K^+, 23 Cl^-	150	no transition	2.0 ± 0.7
revKt-54 (RIB-14)	SPC/E+*ff*99bsc0	46 K^+, 23 Cl^-	65	55	3.2 ± 1.4
revKt-54 (RIB-15)[e]	TIP3P+*ff*99	1 Mg^{2+}, 21 Na^+	150	20	2.5 ± 0.5
revKt-54 (RIB-16)	TIP3P+*ff*99bsc0χ_{OL}	23 Na^+	150	no transition	2.2 ± 0.7
revKt-54 (RIB-17)	TIP3P+*ff*99bsc0χ_{OL}	23 Na^+	150	no transition	1.9 ± 0.4
revKt-54 (RIB-18)	SPC/E+*ff*99bsc0χ_{OL}	46 K^+, 23 Cl^-	150	no transition	1.8 ± 0.4
revKt-54 (RIB-19)	SPC/E+*ff*99bsc0χ_{OL}	46 K^+, 23 Cl^-	150	no transition	2.8 ± 1.4

[a] Some additional MD simulations are listed in Table S3 in the Supporting Information. [b] The initial revKt-P9/9.0 structure in the simulations INT-9, INT-10, INT-15, and INT-16 was taken from the tenth nanosecond of the INT-18 simulation. The initial revKt-54 structure in the simulations RIB-1 to RIB-6 was taken from the *H.m.* 23S rRNA deposited under the code 1S72 while the simulations RIB-7 to RIB-19 were started from the structure taken from the *H.m.* 23S rRNA available under the code 3CC2. [c] Time at which a distorted "ladder-like" conformation of reverse K-turn occurs. [d] The mean RMSD of coordinates with respect to the X-ray structure (see the Methods section for more details concerning the RMSD calculation). The 3CC2 structure is used for revKt-54. The RMSD is strictly calculated over the trajectory portion not affected by the "ladder-like" conformations. [e] One Mg^{2+} ion was included. Its initial position was modeled via replacing the crystal water under ID 7209 in the original 3CC2 23S rRNA with Mg^{2+}. See the Methods section for discussion of the limitations of modeling Mg^{2+} by simple force fields.

Reverse K-turn substantially differs from RNA molecules studied so far by all-atom MD simulations.[35−43] Most RNA MD simulations reported to date studied molecules whose starting structures corresponded to 3D arrangements that are stable *per se*.[44] Representative examples are established autonomous RNA motifs that adopt their structures irrespective of the structural context[45−47] as well as medium-sized noncoding RNAs such as ribozymes,[35,48−51] riboswitches,[39,52] and many other RNAs.[53,54] These molecules stay locked in the starting structures in simulations. They show just local dynamics sometimes accompanied with modest rearrangements of molecular interactions. In some cases, the initial structures are trivially deformed by the surrounding elements that are not included in simulations (for example, bending of helix 44 of the small ribosomal subunit or the GTP-ase associated center RNA of the large subunit).[18,55,56] In such cases, the molecules undergo initial relaxation in simulations, which, however, does not change base pairing and tertiary interactions. Much less frequent are simulations of RNA molecules that should be intrinsically unstable since their functional 3D shapes are induced by their context. One example is the recurrent ribosomal UAA/GAN internal loop, whose 3D structure is completely remodeled by the ribosomal context.[57] This molecule is visibly locally destabilized in simulations but does not spontaneously rearrange anywhere close to the solution structure on a submicrosecond time scale.[58] Similarly, the conventional K-turns are also intrinsically unstable and unfold (unkink) in experiments with an absence of proteins or divalent ions. Nevertheless, the K-turn functional geometry is still locally stable enough so that plain simulations on a 100+ ns time scale so far did not result in any extensive K-turn perturbations or unfolding.[17−22] Considering the sequence, structure, and context of the reverse K-turns, it is obvious that functional (native) reverse K-turn structures also do not correspond to global minima of the respective isolated RNA segments. However, since reverse K-turns are less structured than the conventional K-turns, we might expect visible signs of reversible unfolding and refolding already on the presently affordable simulation time scale. This allows an analysis of force field performance during large-scale RNA rearrangements. Still, the simulations are able to characterize the flexibility of reverse K-turns pertinent to the folded structure, similarly to conventional K-turns. The simulations nevertheless also sample unfolded (or unkinked) and intermediate structures.

METHODS

Studied Systems. Two reverse K-turns were investigated. The initial geometry of revKt-P9/9.0 was taken from the X-ray structure of the *Azoarcus* group I intron with a resolution of 3.1 Å (PDB ID: 1U6B).[28] RevKt-P9/9.0 contains nucleotides 179−188 and 193−205 (23 bases in total; numbering according to the intron X-ray structure). The starting structure of revKt-54 was taken from the 50S ribosomal subunit crystal structures of *Haloarcula marismortui* (*H.m.*) deposited under the PDB codes 1S72 and 3CC2 (both determined at a resolution of 2.4 Å).[32,33] RevKt-54 from 1S72 comprises nucleotides 1516−1531 and 1660−1670 (27 bases), while that of the 3CC2 contains residues 1517−1531 and 1660−1669 (25 bases). The more recent (presumably corrected) 3CC2 structure contains G1669═C1517 and A1670−U1516 while 1S72 contains A1669−U1517 and G1670═C1516 base pairs in the C-stem. We decided to terminate the C-stem with C═G base pair to avoid terminal A−U base-pair fraying,[59] so the terminal C-stem base pair is G1669═C1517 in the case of the 3CC2 system and G1670═C1516 in the case of 1S72. We did not observe any differences between revKt-54 simulations starting from the 1S72 and 3CC2 X-ray structures, and thus we will further discuss all of these simulations as a one-simulation set of revKt-54.

The eubacterial ribosomes reveal that at positions equivalent to revKt-54 of *H.m.*, there are situated segments that bend similarly to the reverse K-turn but with a completely different sequence (hereafter, abbreviated as revKt-54-analogs; Figure S4, Supporting Information). We have carried out one 100-ns MD simulation with the revKt-54-analog from *Escherichia coli* (*E.c.*). The revKt-54-analog starting structure was taken from the X-ray structure (resolution of 3.46 Å) of the *E.c.* 50S large ribosome subunit deposited under the PDB 2AW4, while nucleotides 1405−1424 and 1574−1597 (44 bases in total) were included in the simulation (Figure S5, Supporting Information).[2]

Simulation Setup and Force Field Choice. All MD simulations were carried out using the AMBER[60] suite of programs with several force fields. The *ff*94 and *ff*99 (also known as parm94 and parm99, respectively)[61,62] can be considered as the original parametrizations which slightly differ in sugar pucker and χ torsion parameters. The *ff*99bsc0 (parmbsc0) force field is based on *ff*99 but contains a critical reparameterization of the α/γ torsion parameters, which is essential for stable simulations of DNA molecules[63] and which was recently shown to also modestly improve RNA simulations.[59,64] Until recently, all three force fields were assumed to perform equivalently for RNA systems and provide enough stable simulations on a subhundreds nanosecond time scale.[44,59] However, it has been shown that these force fields do not provide a stable minimum for A-RNA due to imbalanced description of the glycosidic torsion, which tends to adopt a high-*anti* conformation with the subsequent entire degradation of A-RNA systems on a long time scale.[50,64] In fact, some earlier simulation studies including those attempting folding of small RNAs such as stem-loop hairpins are affected by this force field artifact. Thus, complete reparameterization of the glycosidic torsion profile χ_{OL}[64] (parameters are available online at http://fch.upol.cz/en/rna_chi_ol/ (accessed Jan 25, 2010) and have also been included in the most recent *ff*10 AMBER force field as the recommended force field for RNA simulations and released in AmberTools 1.5, the parameterization procedure is in detail described in ref 103) was recently prepared and carefully tested. It prevents the ladder degradation of A-RNA by modifying the *anti* to high-*anti* balance and also improves the *syn* region description.[64] Therefore, in later stages of this reverse K-turn project, we applied the χ_{OL} modification in combination with *ff*99 (labeled as *ff*99χ_{OL}) and *ff*99bsc0 (labeled as *ff*99bsc0χ_{OL}) force fields. In fact, the inclusion of the χ_{OL} correction was entirely critical to adopting the stable trajectories of the present system. Note that although the bsc0 (α/γ) and χ_{OL} parametrizations are independent variants of the force field, our study of RNA tetraloops and short A-RNA stems strongly indicates that χ_{OL} should be combined with *ff*99bsc0 to get the optimal force field behavior.[64]

Ion and Solvent Conditions. Two different ionic (and solvent) conditions were used: the combination of Na^+ counterions (with radius 1.868 Å and well depth 0.0028 kcal/mol)[65] with the TIP3P water model,[66] modeling minimal salt conditions ($c(Na^+)$ of ∼0.25 M) and a higher ionic strength of potassium ($c(K^+)$ of ∼0.5 M, radius 1.870 Å and well depth 0.100 kcal/mol)[67] and chloride ions ($c(Cl^-)$ ∼0.25 M, radius 2.470 Å and well depth 0.100 kcal/mol)[68] in combination with the SPC/E water model[69] to simulate KCl salt excess (Table 1). The monovalent counterions were placed

using the tLEaP program according to the solute electrostatic potential. In addition, some simulations (Table 1 and Table S3, Supporting Information) comprise also divalent magnesium ion/ions coordinated to the reverse K-turn, and the following parameters for Mg^{2+} (radius 0.7926 Å and well depth 0.8947 kcal/mol)[65] were utilized. The rectangular box of explicit water solvent was set, so that a minimum distance between the box wall and the solute was 10 Å. It is to be noted that we did not have any specific reason to systematically combine TIP3P with Na^+ and SPC/E with KCl. We wanted to investigate as broad a set of conditions as possible. Obviously, the limited computer power does not allow us to investigate all possible combinations of parameters while having a statistically significant set of multiple simulations and enough robust sampling. See the Supporting Information for analyses of four simulations (600 ns in total) combining minimal salt conditions of K^+ ions with the SPC/E water model decomposing effects of the water model and salt conditions. Further studies of RNA systems with other ion and water parameters[70,71] are under way. It should, however, be noted that in general the ion/water parameters and conditions do not have a decisive effect on nucleic acids simulations, as their outcome is primarily determined by the solute force field. The present system, due to its flexibility, is assumed to be potentially more sensitive to ion/water conditions than other nucleic acids systems.

Prior to the production phase of the MD simulation, each system was minimized and subsequently warmed up to 298 K as follows. The RNA molecule was constrained, and the solvent molecules with counterions were allowed to move during a 1000-step minimization followed by 10-ps-long MD runs under $[NpT]$ conditions (p = 1 atm, T = 298.15 K). The solute was then relaxed through several minimization steps, with decreasing force constants applied to the backbone atoms. After the relaxation, each system was heated to 298.15 K within 100 ps. The particle-mesh Ewald (PME) method[72,73] was used for treating electrostatic interactions, and all simulations were performed under periodic boundary conditions in the $[NpT]$ ensemble at 298.15 K and 1 atm using a 2 fs integration step. The SHAKE algorithm with a tolerance of 10^{-5} Å was used to fix positions of all hydrogen atoms. A 10.0 Å cutoff was applied to nonbonding interactions, and coordinates were stored every picosecond. Together, 30 independent simulations (Table 1 and Table S3, Supporting Information), each 150-ns-long, were carried out with revKt-P9/9.0, and 19 simulations (Table 1) on the 40+ ns time scale were carried out with revKt-54. In addition, four independent 150 ns MD simulations were carried out with revKt-P9/9.0-A201G (revKt-P9/9.0 with A201G mutation), and one 100 ns simulation was conducted with the 23S rRNA *E.c.* revKt-54-analog (Table S3, Supporting Information). The cumulative production time amounts to ~7.4 μs.

Data Analysis and Description of Topology. MD trajectories were analyzed with the Ptraj module of the AMBER package. PyMOL[74] and VMD[75] programs were used for visualization and preparation of figures.

The RMSD vs R_g density plots were calculated using an *in-house* script. An array of 150 × 150 bins was used. The scale on the right-hand side of the density plots indicates the relative occurrence of structures in the corresponding bin. The RMSD was mass-weighted and computed over all atoms of nucleotides 180−188 and 193−204 in the case of revKt-P9/9.0 and nucleotides 1518−1530 and 1661−1668 in the case of revKt-54. The X-ray structure of revKt-P9/9.0 was used as a reference structure for the RMSD calculations. However, the simulations of revKt-54 revealed a more compact conformational substate in comparison with its X-ray structure, which may be a consequence of removing the motif from its structural context. Thus, the average structure of this more compact substate (labeled as B′ in the text, see the Results section) was used for the RMSD analysis in the case of revKt-54 (see Supporting Information, Figure S1B for the density plot in which the RMSD is calculated with respect to the X-ray structure).

The compactness of the reverse K-turns structure was described using the end-to-end distance. The end-to-end distance equals the distance between the centers of mass of selected C-stem and NC-stem terminal nucleotides of the respective reverse K-turn (Figure S2, Supporting Information). The center of mass of the revKt-P9/9.0 C-stem terminus included nucleotides G186, G187, C194, and C195, while that of the NC-stem included G180, G181, C203, and C204. The revKt-54 C-stem terminus center of mass included A1518, U1519, A1667, and U1668, while the NC-stem terminus involved G1529, U1530, A1661, and C1662. For each reverse K-turn, the lowest end-to-end distance corresponds to a highly kinked structure, while the largest value denotes an unkinked (extended) structure.

In addition, we attempted to describe the global molecule topology using two additional structural parameters: the interhelical angle and the interhelical dihedral calculated using a recently proposed algorithm.[76] The mathematical definition of both structural parameters is given in the Supporting Information (see Supporting Information, Figure S2 and Table S2). However, the opening of reverse K-turns is a rather complex structural rearrangement that cannot be fully described by these two parameters modeling the system as two (almost) rigid stems connected by a hinge. Instead, all six degrees of freedom describing mutual orientation of stems in space seem to be crucial for the description of global structural dynamics of reverse K-turns (see Supporting Information).

Qualitative analysis of energy differences among reverse K-turns substates was carried out using the MM-PBSA (Molecular-Mechanics, Poisson−Boltzmann Surface Area) module of AMBER 11.[60,77] The Gibbs energy of solvation was calculated by both Poisson−Boltzmann[78] and generalized Born[79] implicit solvent models, while the entropy contribution was estimated from normal-mode analysis. MM-PBSA allows one to estimate free energies by postprocessing explicit-solvent simulation trajectories. The energy differences should be interpreted with care, because the validity of the MM-PBSA method for RNA is compromised by the inaccuracy of implicit solvent models for the polyanionic chain of RNA, as was, e.g., demonstrated by rapid degradation of the *glmS* riboswitch in implicit solvent MD simulations.[51] The essential dynamic analysis (EDA) was carried out using the GROMACS program.[80] All atoms of revKt-P9/9.0 residues 180−188 and 193−204 and revKt-54 residues 1518−1530 and 1661−1668 were included in the EDA calculations. The projections onto the first five essential modes were computed and subsequently visualized in the PyMOL program.

RESULTS

Starting Structures. The reverse K-turns consist of an internal bulge of unpaired bases (kink region, nucleotides 198−200 for revKt-P9/9.0 and 1522−1526 for revKt-54) flanked by canonical C-stem and noncanonical NC-stem (Figures 1 and 2). The overall fold of both studied reverse K-turns is bent resembling an "L"- or "V"-shaped structural motif of K-turns.[1]

However, reverse K-turns are bent in the opposite direction of K-turns, i.e., toward major grooves (Figure 1). Furthermore, while the topology of conventional K-turns is roughly uniform, the X-ray structures of reverse K-turns substantially differ (Figure 1). The structure of revKt-P9/9.0 is more compact, showing a smaller end-to-end distance (Table 2) and base-phosphate (BPh)[81] interactions between the bulge and NC-stem (Figure 2) in comparison to the more extended revKt-54 structure.

There is one magnesium ion resolved in the revKt-P9/9.0 X-ray structure coordinated to G181 (by inner-shell contact) and G182 (an outer-shell interaction) bases, additionally forming an inner-shell contact with one water molecule (Figure 2A). Although a Mg^{2+} ion is not present directly in the kink region, it is close enough to potentially provide some electrostatic stabilization, which could compensate for the repulsion between C- and NC-stems' phosphates. In contrast, no divalent cation was resolved in the revKt-54 crystal structure, although it still does not rule out the presence of a cation in this region, since cations can be disordered and elude detection.[49,82,83]

Table 2. End-to-End Distance of Reverse K-Turn Crystal Structures and Average Structures of the Relevant Substates Obtained from MD Simulations (See Figure 5)

	end-to-end distance (Å)	
structure type	revKt-P9/9.0	revKt-54
crystal structure	20.2	26.9
substate A/A′	19.4	19.8
substate B/B′	22.9	23.0
substate C/C′	28.6	26.6
substate D/D′	31.2	29.8

The revKt-P9/9.0 contains four 6BPh interactions (6BPh interaction is a hydrogen bond between the amino group of either adenine (N6) or cytosine (N4) and the phosphate oxygen[81]). Two 6BPh contacts are formed by revKt-P9/9.0 internal bulge bases A198 and C199 with the G180 phosphate of the NC-stem (henceforth, named the bulge-helix BPh contacts), while the next two 6BPh interactions are literally cementing the *t*HH A201/A183 base pair of the NC-stem (Figure 2A). In contrast, only one 6BPh interaction occurs in the revKt-54 system, being formed between the bases A1527 and A1664 of the NC-stem (Figure 2B), i.e., again stabilizing the *t*HH base pair flanking the internal bulge.

RNA−RNA Tertiary Interactions and Structural Context of Reverse K-Turns. Neither of the studied reverse K-turns binds any proteins,[31] but both of them are affected by RNA−RNA interactions. The revKt-P9/9.0 is accompanied by the formation of a tetraloop−tetraloop receptor (TL-TLR) interaction between atoms of the GNRA tetraloop (nucleobases 189−192) flanking the revKt-P9/9.0 C-stem and the P5/5a segment of the group I intron (Figure 2A). This contact is assumed to be responsible for the bending of this reverse K-turn.[29] The 23S *H. m.* revKt-54 is not associated with any TL-TLR contact but is stabilized by the interaction between four adenines A1656−A1659 of the revKt-54 NC-stem and the minor groove of the A-RNA duplex (part of helix 52 between the UAA/GAA internal loop and adjacent four-way junction; residues 1455−1457, 1485, and 1489−1490; Figure 3). Interestingly, equivalent regions of eubacterial revKt-54-analogs show the same RNA−RNA interaction (Figure S6, Supporting Information) despite the reverse K-turn not being conserved. The sequence and the 3D structure of this tertiary interaction are strictly evolutionarily conserved in the ribosome (Figures 4A−D). This tertiary contact can play an important role in revKt-54

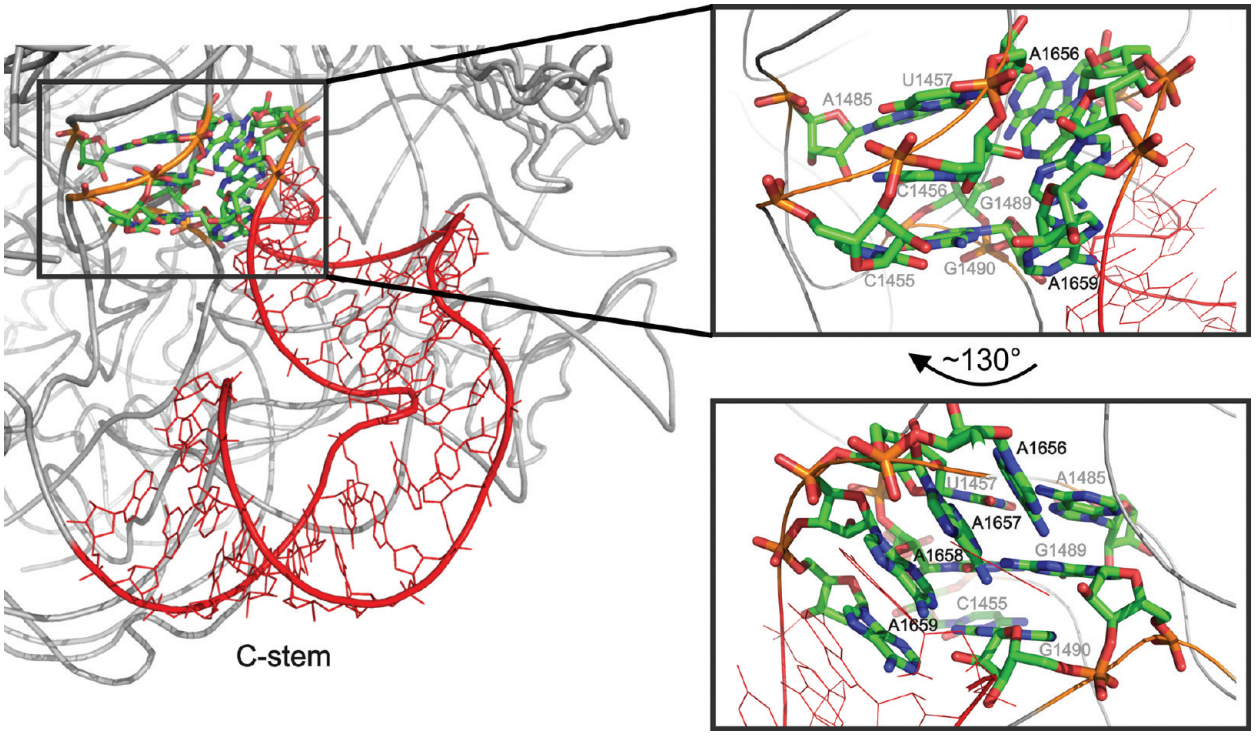

Figure 3. The tertiary RNA−RNA contact formed between the four adenines (A1656−A1659) of the revKt-54 NC-stem and part of helix 52 (base pairs *t*HW A1485/U1457, *c*WW G1489═C1456, and *c*WW G1490═C1455).

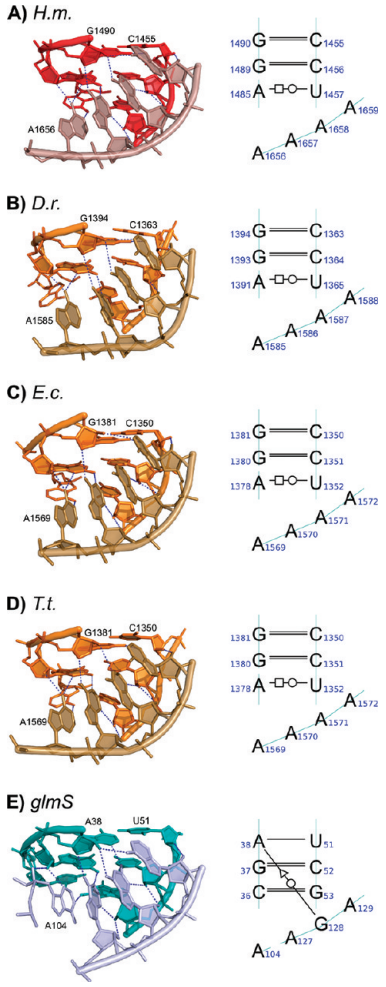

Figure 4. Three-dimensional (left) and secondary structures (right) of the new unclassified RNA interaction motif from 23S rRNAs of *Haloarcula marismortui* (PDB 3CC2) (A), *Deinococcus radiodurans* (PDB 1NKW) (B), *Escherichia coli* (PDB 2AW4) (C), and *Thermus thermophilus* (PDB 2J01) (D). (E) Depicts the motif isosteric to the rRNA motifs located in the *glmS* riboswitch (PDB 2HO7).

bending similarly to the TL-TLR interaction in revKt-P9/9.0 bending.

Transition of Reverse K-Turns' Helices into Senseless "Ladder-Like" Conformation with *ff*94, *ff*99, and *ff*99bsc0 Force Fields. MD simulations carried out with the common AMBER family force fields *ff*94, *ff*99, and *ff*99bsc0 show that both helices of each reverse K-turn undergo irreversible rearrangement to a "ladder-like" conformation (Figure S7, Supporting Information). The "ladder-like" structure was first identified as a force field artifact in extensive MD simulations of the hairpin ribozyme.[50] It was subsequently detected in simulations of short A-RNA stems and stem-loop systems.[64] The degraded "ladder-like" stem has in comparison with the A-RNA duplex a reduced twist from ∼33° to ∼10°, a base pair slide shifted from ∼−2 to ∼4 Å, and glycosidic torsions χ fluctuating around or even outside the high-*anti* region (i.e., ∼−90° while typical A-RNA χ value is ∼−165°). The shift of glycosidic torsion to a high-*anti* region is the most evident feature of the "ladder-like" structure. Considering these data and our previous simulations,[50,64] we can conclude that this artifact may be rather widespread in long *ff*94, *ff*99, and *ff*99bsc0 simulations of RNA molecules with exposed terminal stems. In fact, our unpublished simulations indicate that even folded RNA molecules sooner or later degrade toward high-*anti* structures if the simulations are long enough. The formation of "ladder-like" structures occurred stochastically, generally on a time scale of tens of nanoseconds (Table 1), and was entirely irreversible.

We did not observe any effect of ionic condition (net-neutralizing Na^+, K^+, and KCl salt excess) or the used water model (TIP3P and SPC/E) on the formation of the "ladder-like" structure, so this artifact seems to be solely a consequence of solute force field parameters. As noted above, although water/ion/salt parameters and conditions may sometimes influence NA simulations, the outcome of the simulations is overwhelmingly determined by the solute force field.

In contrast, no formation of "ladder-like" structure was observed with the new χ_{OL} parametrization of glycosidic torsion parameters, i.e., when applying the *ff*99χ_{OL} and *ff*99bsc0χ_{OL} force fields.[64] The density plot RMSD vs R_g calculated from all *ff*99χ_{OL} and *ff*99bsc0χ_{OL} productions (cumulative time of 1.1 μs for revKt-P9/9.0 and 0.6 μs for revKt-54) almost perfectly matches the RMSD vs R_g plot computed over *ff*94, *ff*99, and *ff*99bsc0 trajectory portions before the "ladder-like" degradation occurs (1.4 μs for revKt-P9/9.0 and 1.2 μs for revKt-54; Figure S8, Supporting Information). Thus, when using MD simulations carried out with *ff*94, *ff*99, and *ff*99bsc0 force fields, only trajectory portions before the "ladder-like" formation events were considered relevant for analysis of the conformational properties of reverse K-turns. Fortunately, we have accumulated enough data without this major artifact to characterize flexibility of the studied system. The "ladder-like" stem distortions are easily detectable as artificial substates in the RMSD vs R_g plots (Figure 5).

In summary, reverse K-turn simulations with corrected glycosidic torsion parameters agree with *ff*94, *ff*99, and *ff*99bsc0 simulations before the later simulations degrade, while the new parameters entirely prevent the "ladder-like" structure degradation. Thus, the reverse K-turn structures could finally be analyzed using 4.3 μs of "healthy" data.

Structures of revKt-P9/9.0 and Their Evolution over MD Simulations. The RMSD vs R_g density plot (Figure 5A) calculated from all of the 150 ns revKt-P9/9.0 simulations (2.7 μs in total) shows seven significantly populated structural substates. Yellow boxes highlight those revKt-P9/9.0 substates that are free of the "ladder-like" conformations (A−D) and which are therefore relevant for further analyses. The gray boxes mark the revKt-P9/9.0 substates with the NC-stem (substates E and G) or the C-stem (substate F) in the distorted "ladder-like" conformation.

Figure 6A illustrates the overall shape ("topology") of the average structures for the relevant substates A−D. The topology of the most compact substate A is nearly identical to that of the X-ray structure (Figure 6A and Figure S9, Supporting Information). On the other hand, substate D corresponds to a fully unfolded (unkinked) revKt-P9/9.0 (cf. Figure 6A and Table 2). The other substates B and C represent intermediate states between the native-like kinked and fully unkinked conformations (Table 2). In particular, substates B and C exhibit high flexibility corresponding to a bending movement, which is responsible for the elongated ellipsoidal shape of the corresponding regions in the density plot (see Figure 5A). Two BPh interactions supporting the *t*HH A/A base pairs remain stable during the whole simulations in all substates. In contrast, the other two bulge−helix BPh interactions observed in the X-ray structure and in substate A are much less populated in substate B and disappear in

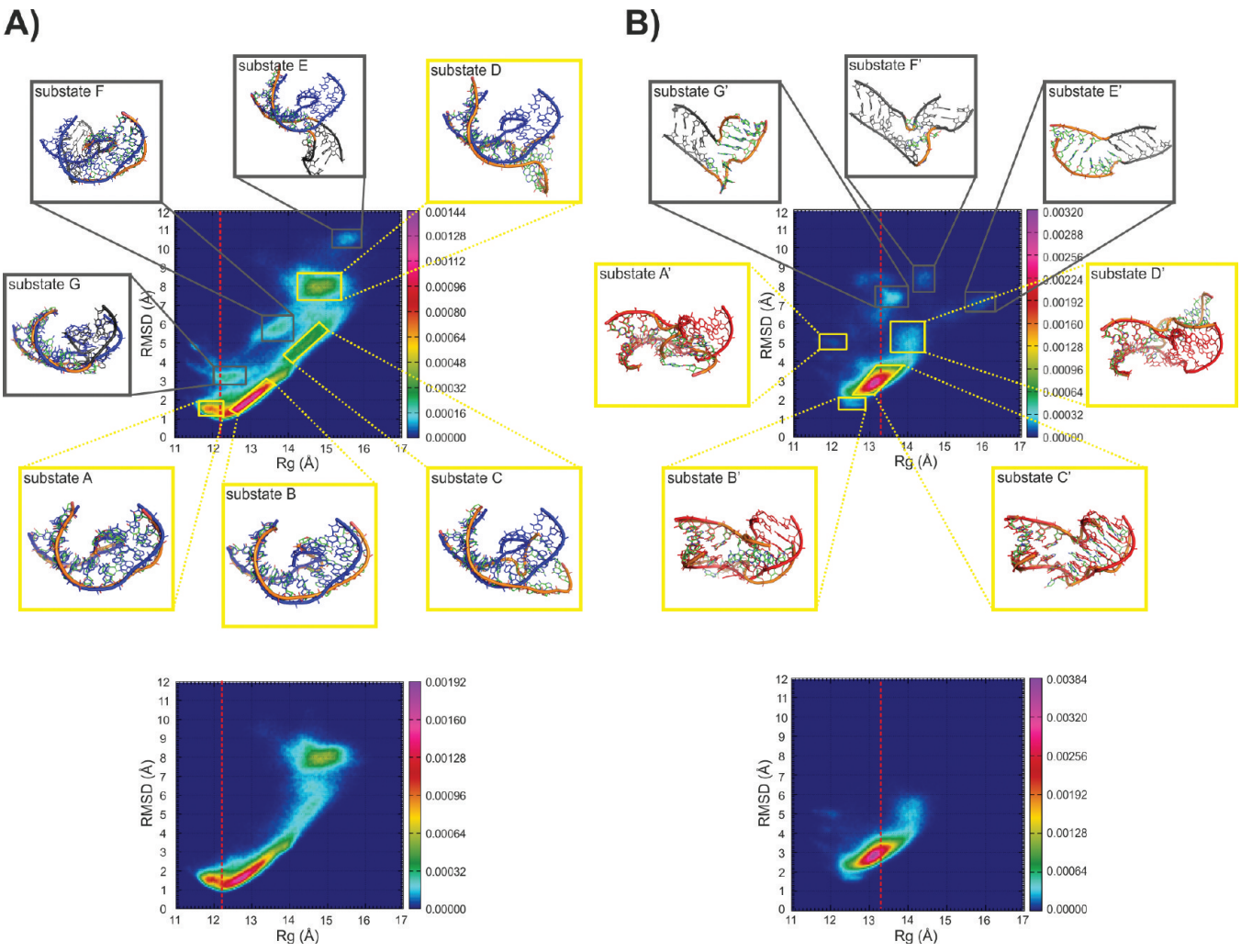

Figure 5. The upper parts of panels A and B show RMSD vs R_g density plots calculated over the entire trajectories of all revKt-P9/9.0 and revKt-54 simulations listed in Table 1, respectively. The yellow frames show densely occupied "healthy" regions of the RMSD vs R_g plots and the corresponding structure representatives (substates A−D and A′−D′). Gray boxes show substates and their representative structures bearing the degraded "ladder-like" conformation (substates E−G and E′−G′, nucleotides within the "ladder-like" conformation are colored in gray). The C-stems of each structure representative are superimposed over the C-stem of the starting structure of revKt-P9/9.0 in blue and revKt-54 in red, respectively (except of substates F and E′−G′). The vertical dashed red line highlights the radius of gyration of the crystal revKt-P9/9.0 and revKt-54 structures. In the lower part of panels A and B are the same density plots for revKt-P9/9.0 and revKt-54, respectively, but visualized without the trajectory portions affected by the "ladder-like" reverse K-turn conformations.

the more unkinked structures of substates C and D (Table 3). Besides that, the X-ray stacking pattern of bases C199 and A200 is reasonably well preserved in substates A and B, while in the substates C and D, the respective bases favor various non-native geometries (not shown).

The fully unfolded substate D almost vanishes in the MD simulations carried out with the excess KCl salt and SPC/E water model except for one MD run, INT-25, in which a reversible transition to substate D occurs, with substate D persisting for several nanoseconds (cf. Figure 7A for the time evolution of substates in all MD simulations). On the other hand, almost all MD simulations conducted with the net-neutralizing Na^+ ions and TIP3P water model sample all conformational substates A−D. This is most likely the consequence of the different viscosities of the TIP3P and SPC/E water model rather than being caused by the different ion parameters and concentrations (see the discussion about the effect of water models below). The transitions from the fully kinked substate A to the fully unkinked substate D (and vice versa) usually pass through substates B and C. The transitions between substates usually occur on the time scale of several nanoseconds. Notably, revKt-P9/9.0 fully unfolds also in the presence of Mg^{2+}.

Structures of revKt-54 and Their Evolution over MD Simulations. Seven densely populated regions were identified in the revKt-54 density plot (Figure 5B). Three of them contain "ladder-like" artificial conformations (substates E′−G′) and are not further discussed. The remaining four substates (A′−D′) exhibit relevant structures without the "ladder-like" distortion.

Substates A′ and D′ represent the most compact (kinked) and the most extended (unfolded/unkinked) revKt-54 structures, respectively (Table 2; Figures 5B and 6B). Just as for substates B and C of revKt-P9/9.0, substates B′ and C′ correspond to intermediates between the kinked and unkinked states (Figure 6B). Similarly to intermediate substates B and C of revKt-P9/9.0,

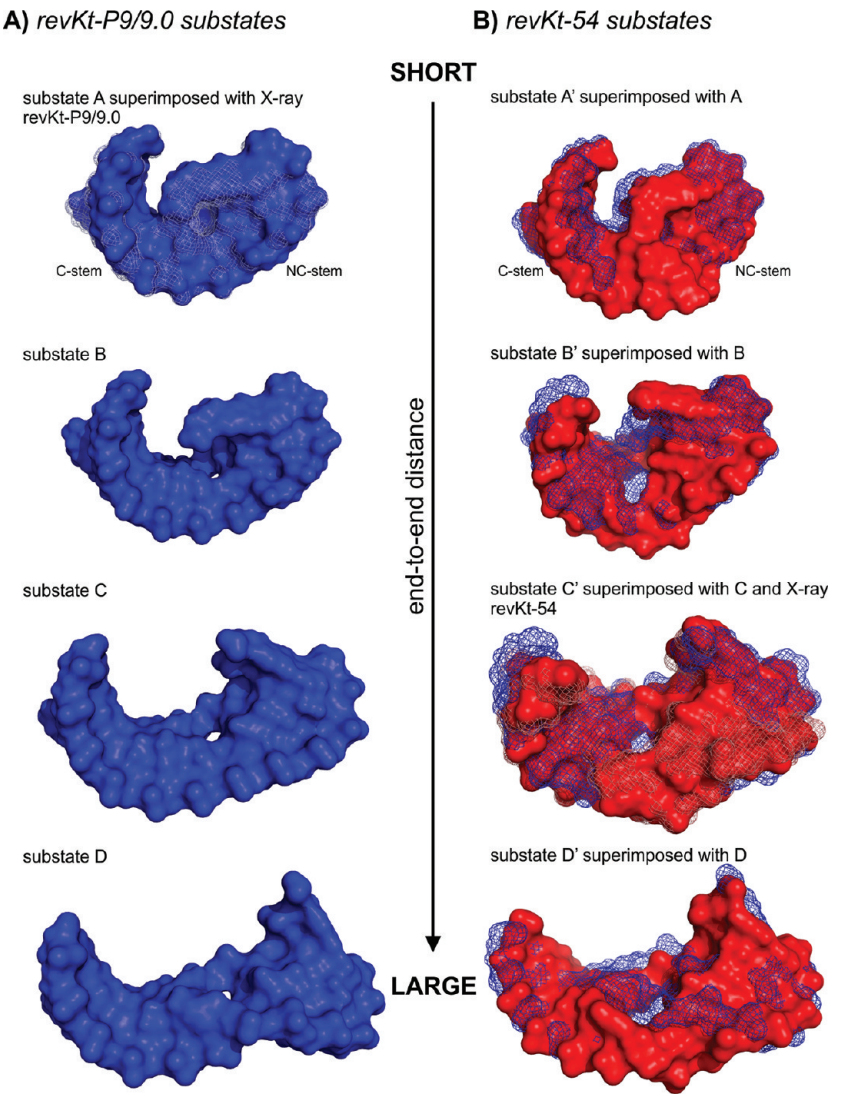

Figure 6. Average structures of revKt-P9/9.0 substates A—D (left) and revKt-54 substates A′—D′ (right) visualized using the surface representation. Blue mesh representation on the right represents revKt-P9/9.0 substates superimposed over the C-stem and NC-stem backbone atoms with corresponding revKt-54 substates. In addition, gray mesh structures superimposed over substates A and C′ of revKt-P9/9.0 and revKt-54, respectively, correspond to their X-ray structures.

Table 3. Stability of revKt-P9/9.0 BPh[81] Interactions in Substates Calculated As a Relative Population of H Bonds Involved in the BPh Interaction with a 4.0 Å for Cutoff Distance between Heavy Atoms (in %)[a]

substate	A198(N6)—G180(O1P)	C199(N4)—G180(O2P)	A201(O2P)—A183(N6)	A183(O1P)—A201(N6)
A	34.5	35.1	97.9	60.5
B	10.0	9.7	89.5	68.7
C	0.0	0.0	31.2	72.2
D	0.0	0.0	67.2	71.1
X-ray (Å)	3.3	2.9	2.7	3.2

[a] The X-ray H-bond distances are in the last line.

substate C′ of revKt-54 reveals intrinsic bending movement represented by an ellipsoidal, elongated population in the density plot (Figure 5B). The average structure of substate C′ resembles the X-ray revKt-54 topology (Figure 6B and Figure S10, Supporting Information). Similar to revKt-P9/9.0, the 6BPh interaction supporting the *t*HH A/A base pair is present in all structural substates (26%, 63%, 47%, and 73% population of direct H-bonding in substates A′, B′, C′, and D′, respectively). Substate C′ maintained well the native stacking pattern of the kink region bases, with only U1524 occasionally flipping out (data not shown), while the native conformation of kink region bases is distorted in other substates, A′, B′, and D′.

Substate C′, resembling the X-ray topology, is significantly populated over the entire time scale of most revKt-54 MD simulations (Figure 7B). In contrast, the fully kinked substate A′ is only negligibly populated in our simulations; namely, it is propagated for only several nanoseconds in the MD run RIB-19 (excess KCl salt and SPC/E water). The only substantial occupancy of substate B′ was observed in the simulation with 12 Mg^{2+} ions and TIP3P water (RIB-2). Unfolding of revKt-54 to substate D′ was detected in two simulations with Na^+ ions and the TIP3P water

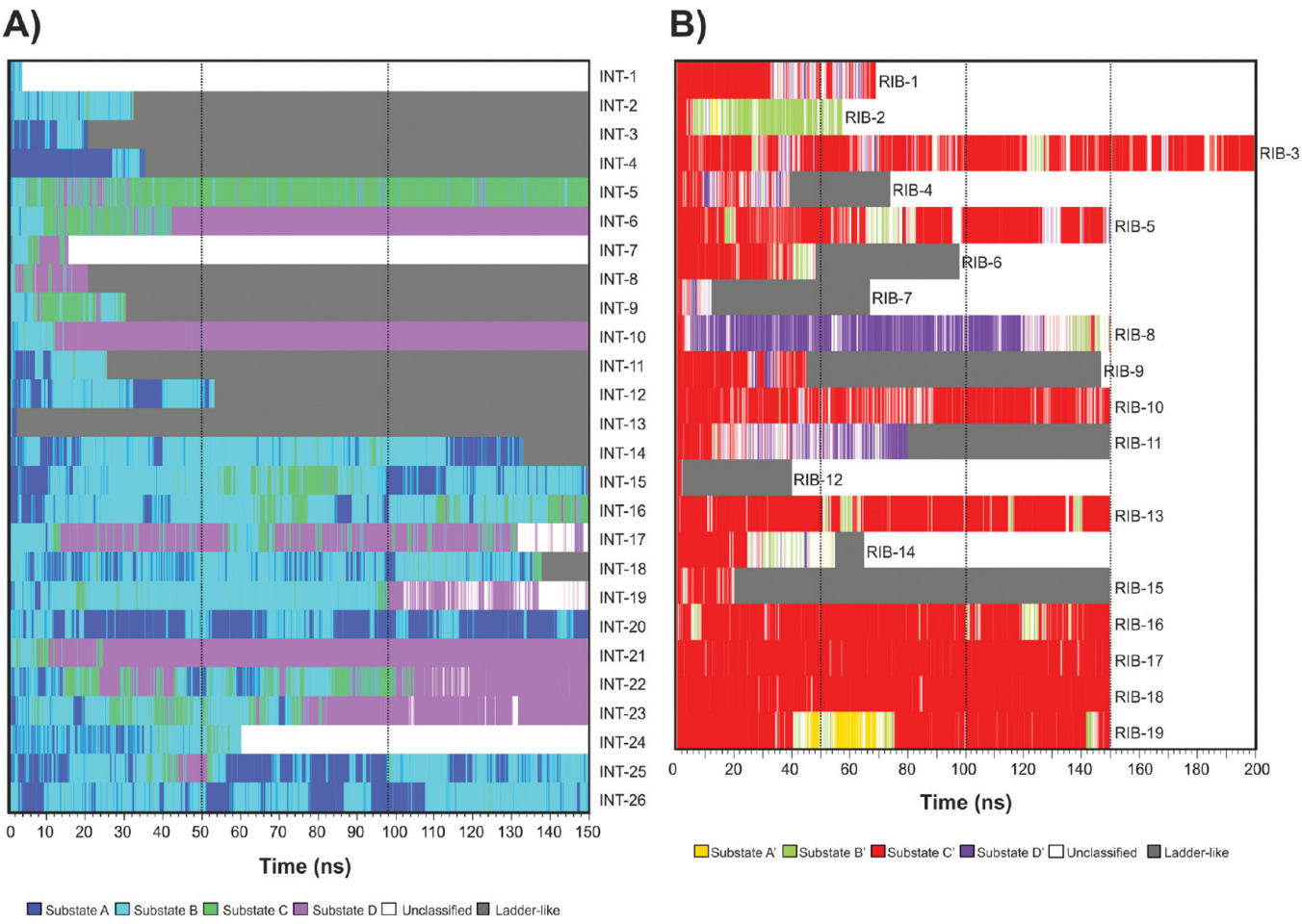

Figure 7. Time evolution of revKt-P9/9.0 (A) and revKt-54 (B) substates in individual MD simulations. The ends of individual simulations are marked by the simulation labels that correspond to Table 1.

model (RIB-8 and RIB-11; see Figure 7B). The refolding of revKt-54 from substate D′ through C′ toward B′ was observed in the RIB-8 simulation. Thus, similar to revKt-P9/9.0 simulations, the transition of revKt-54 toward more extended structures represents a fully reversible process on our simulation time scale.

Topological Similarity among the revKt-P9/9.0 and revKt-54 Substates. Although the sequence and topology in the X-ray structure of both studied reverse K-turns differ substantially, the simulations reveal profound similarity in large-scale dynamics of these motifs when they are removed from their structural context. This can be considered as a flexibility signature of the reverse K-turn. We found that both reverse K-turns share very similar structural substates (A−D and A′−D′ for revKt-P9/9.0 and revKt-54, respectively) sampled in MD simulations (Figure 6). Although the simulations of each system started from a different conformational substate due to differences between their X-ray structures (the X-ray structures of revKt-P9/9.0 and revKt-54 correspond to substates A and C′, respectively), both systems finally sample all four substates (Figure 7). Figure 6 summarizes structural similarities between conformational substates of both reverse K-turns. The most compact substates (A and A′) have small values of the end-to-end distance, while unfolded (unkinked) substates (D and D′) are characterized by the largest end-to-end distance (Table 2). The intermediate substates (substate B and C of revKt-P9/9.0 and substate C′ of revKt-54) correspond to a rather broad range of geometries with high hinge-like flexibility (see Figures 5 and 8 and the next paragraph), while the most compact or the most extended substates reveal only minor dynamics corresponding to local fluctuations around energy minimal conformation.

Both Reverse K-Turns Have Overall Hinge-Like Flexibility Similar to K-Turns. The essential dynamics analysis (EDA) reveals that the first essential motions of substates B and C of revKt-P9/9.0 and substate C′ of revKt-54 resemble the hinge-like dynamics observed in MD simulations of conventional K-turns[17−20] (Figure 8). The first essential motions dominate over the other modes, and they contribute 25.0, 34.4, and 28.5% of essential dynamics of revKt-P9/9.0 substates B and C and revKt-54 substate C′, respectively. The contributions of the subsequent essential motions progressively decrease (Table S4, Supporting Information). The hinge-like motion can be qualitatively described as a motion of two rather rigid helical arms caused by the flexible kink region. The observed motion of reverse K-turns substates B, C, and C′ exhibits anisotropic dynamics. The hinge-like dynamics of these substates is also coupled with the local dynamics of kink region bases (bases C199 and A200 in substate B, A198 in substate C, and U1524 in substate C′, see Figure 8). Substate C hinge-like dynamics is additionally coupled with *c*WW G184═C197 base pair propeller twist fluctuation. The ellipsoidal, elongated population region of these substates

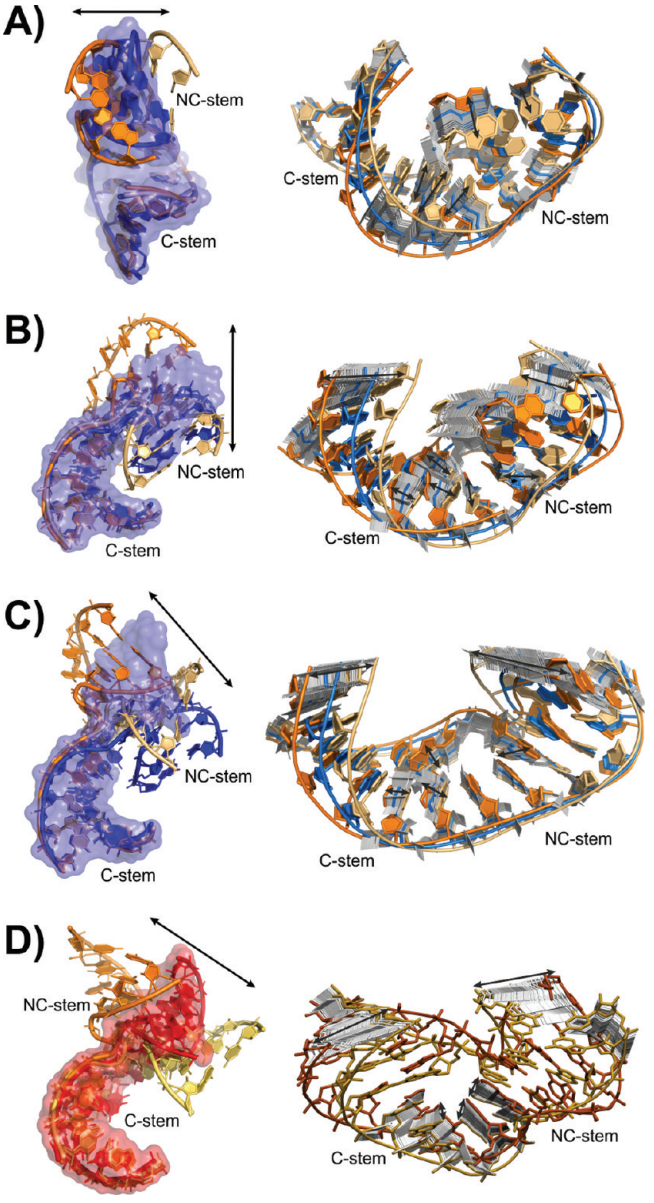

Figure 8. Essential dynamics analysis. The first essential modes of revKt-P9/9.0 substates A, B, and C (panels A, B, and C, respectively) and revKt-54 substate C′ (panel D). Figures on the left illustrate magnitudes of the hinge-like oscillations for the respective substate. The panels show superposition (over the C-stem) of the two extremes of essential mode (in orange and light-orange) with the average (surface representation) and initial reverse K-turn structure (cartoon representation). The initial and average revKt-P9/9.0 structures are colored in blue, while the initial and average structures of revKt-54 are in red. Figures on the right illustrate the coupling between the hinge-like fluctuations and local motions of bulge bases (as highlighted by the black arrows).

(Figure 5) is likely caused by this hinge-like dynamics identified by EDA. In other words, in this particular case, we were capable of identifying the movement revealed by the EDA also in the full simulation, which is not always possible due to approximations inherent to EDA.[56] A very similar hinge-like dynamics was also observed in the simulation of the *E.c.* revKt-54-analog (nucleotides 1407−1422 and 1576−1595 of 2AW4 PDB). This suggests that although the reverse K-turn is not conserved in eubacteria, the equivalent RNA segments in eubacteria still show conservation of basic RNA topological and dynamical features (Figure S11, Supporting Information).

Substates B and C of revKt-P9/9.0 and C′ of revKt-54 are similar from the flexibility point of view. However, while substate C′ fluctuates around the X-ray geometry of revKt-54, neither substate B nor substate C is the native state of revKt-P9/9.0 (Figure 8). The X-ray conformation of revKt-P9/9.0 corresponds rather to the structurally more compact substate A, which does not show much bending flexibility. Instead, there are some "side-to-side" fluctuations of revKt-P9/9.0 substate A coupled to the formation/loss of the bulge−helix BPh interactions (Figure 8A). Similarly to substate A of revKt-P9/9.0, a low flexibility was identified for structurally compact substates A′ and B′ of revKt-54, albeit they are only marginally sampled in our study (see Figure 7B). This may reflect the difference in compactness of the starting structures of both reverse K-turns, which obviously still affects sampling on the present simulation time scale. Consistent with the analogy between substates A and A′ of both reverse K-turns, we noticed a 4BPh interaction in poorly populated substate A′ of revKt-54, which is formed between the G1523 (situated in the kink region) and A1661 phosphate of the NC-stem. Thus, substate A′ reveals an internal revKt tertiary contact which seems to be analogous to the native bulge−helix BPh contacts visible in revKt-P9/9.0.

In summary, the results show that the conformational space of reverse K-turns consists of four substates ranging from compact closed to open unkinked geometries. Interestingly, while the intron molecule captures or utilizes the reverse K-turn in its most closed geometry, the ribosome utilizes the semiclosed structure, which is intrinsically the most flexible one. The archaeal ribosomal revKt-54 is replaced in eubacteria by seemingly unrelated sequences, which nevertheless adopt a similar shape and share the anisotropic flexibility.

Water Model Affects revKt-P9/9.0 Conformational Behavior. RevKt-P9/9.0 generally fully unfolds (occupies more frequently the substate D topology) in simulations carried out with TIP3P water model and net-neutralizing Na^+ ions ($c(Na^+)$ ∼0.25 M; Figure 7A and Figure S12, Supporting Information). In contrast, all MD simulations carried out with the SPC/E water model and the KCl excess salt ($c(K^+)$ ∼0.5 M; $c(Cl^-)$ ∼0.25 M) conditions maintain the kinked conformation of revKt-P9/9.0. Thus, we performed an additional set of MD simulations carried out in net-neutralizing K^+ ions ($c(K^+)$ ∼0.25 M and SPC/E water model, listed in Table S3 in the Supporting Information). We observe the same behavior in these simulations as for SPC/E KCl salt excess simulations (Figure S12, Supporting Information), explicitly suggesting that the differences in behavior are not due to different ionic conditions (K^+ net neutralizing and KCl salt excess). Further, although we have taken the Na^+ and K^+ parameters from different sets of cation parameters (see Methods), we observed that the Na^+ and K^+ ions occur at identical binding sites and with the same occupancy in the net-neutralizing (∼0.25 M) Na^+ and K^+ simulations (Figure S13, Supporting Information). This suggests that differences in behavior among revKt-P9/9.0 simulations most likely do not originate in the type of ions (Na^+ vs K^+ ions) but are driven by water models (TIP3P vs SPC/E). We can hypothesize that the effect of solvent model on the reverse K-turn flexibility can have two reasons, kinetic and thermodynamic. The TIP3P model has an approximately 2 times larger self-diffusion constant than SPC/E,[84] so the unfolding of revKt-P9/9.0 can be accelerated in TIP3P in comparison with SPC/E simulations.

Qualitative analysis of free energy differences among the substates carried out using the standard implicit solvent MM-PBSA free energy method shows that the compact states (A, B, A′, and B′) differ from the open states (C, D, C′, and D′) in Gibbs energy of solvation and the electrostatic term (Table S5, Supporting Information). The compact states are destabilized by the electrostatic term, due to repulsion of the phosphates, which is compensated by a more favorable Gibbs energy of solvation. This might indirectly support the idea that the observed differences in populations of reverse K-turn substates in explicit solvent simulations could also be caused by a different Gibbs energy of solvation between the TIP3P and SPC/E explicit water models. Nonetheless, larger time scale simulations with the SPC/E water model would be required to verify this hypothesis. Work is in progress to provide further insights into this issue. Nevertheless, it is so far apparent that selection of the water model has a much larger impact on these simulations than selection of the type and concentration of ions.

Divalent Mg^{2+} Ions Do Not Stabilize Reverse K-Turns' Kinked Topology. We carried out a set of simulations of both reverse K-turns with Mg^{2+} ions to test the influence of divalents on the flexibility of reverse K-turns. Six simulations of revKt-P9/9.0 were carried out with the TIP3P model and one Mg^{2+} ion settled near the kink region. In three out of these six simulations (INT-18, INT-19, and INT-S8), we observed unfolding of the system to substate D, i.e., similar behavior as observed in simulations with monovalent ions. The unfolding occurred on a 10 ns time scale and was entirely irreversible. Similarly, only one of four MD simulations of revKt-54 carried out with divalents revealed a stabilizing effect in the B′ substate (Figure 7B). Taken together, we did not observed any statistically relevant effect of divalent ions on the dynamic behavior of reverse K-turns. Nonetheless, it should be noted that these conclusions are limited, as classical empirical nonpolarizable force fields describe divalents inaccurately and divalents sample poorly in simulations. Thus, we generally do not recommend to include divalents in nucleic acids simulations, unless absolutely critical due to structural reasons.[44,49,55,85] The total amount of polarization and charge-transfer nonadditivities in the first ligand shell of a divalent cation (contributions entirely lacking appropriate terms in common biomolecular force fields) is about 70 kcal/mol. These effects obviously further propagate far beyond the first ligand shell, dramatically affecting the neighborhood of the divalent cation. In other words, for divalent cations such as Mg^{2+}, the force field approximation essentially breaks down completely.[86−91]

DISCUSSION AND CONCLUSIONS

Reverse K-turns are RNA motifs that possess significant sequence similarity to the conventional K-turns but have a very different mutual arrangement of the A-RNA duplexes (stems). The stems of conventional K-turns are aligned in such a way that their minor grooves are juxtaposed. The reverse K-turns display an opposite stem bending with juxtaposition of the major grooves (Figure 1). There is no significant H-bonding between stems of reverse K-turns, in contrast to K-turns that are stabilized by signature interactions.[1] To date, three unique reverse K-turns have been found in the available RNA structural data.[31,34] We studied the reverse K-turn occurring in the *Azoarcus* group I intron (revKt-P9/9.0)[28] and the reverse K-turn of helix 54 in the 23S rRNA of *H.m.* (revKt-54).[31]

We present an extensive set (7.4 μs) of explicit solvent MD simulations carried out for isolated reverse K-turns. Such simulations capture the internal flexibility of the studied RNA motifs pertinent to their starting structures, which correspond to the native folded arrangement.[44] The simulations were conducted with the traditional AMBER Cornell et al. force fields *ff*94, *ff*99, and *ff*99bsc0. Additional simulations were conducted with the recently reparameterized nucleotide N-glycosidic torsion profiles (χ_{OL}), which became available in the course of the project.[64] These simulations are labeled as either *ff*99χ_{OL} or *ff*99bsc0χ_{OL}, depending on whether the bsc0 correction is used or not (Table 1 and Table S3, Supporting Information). The simulations also compare different ion conditions (minimal concentration of Na^+ or K^+, Na^+ ions combined with Mg^{2+} divalents, and, finally, KCl excess salt). Two different explicit water models (TIP3P and SPC/E) are utilized in this study. Thus, besides the initial aim to examine the intrinsic stability and flexibility of reverse K-turns, our study also provides valuable insights into the force field dependence of RNA simulations. Due to the unique propensity of reverse K-turns to show structural transitions on the short time scale of simulations, these RNA systems are useful in such force field studies.

The Effect of the Solute Force Field on Stability of Trajectories. Without using the χ_{OL} parametrization, the stems of both reverse K-turns structurally degrade by adopting a distorted "ladder-like" conformation (Figure 5 and Figure S7, Supporting Information). The "ladder-like" conformation was recently identified as a major force field artifact which is associated with transition of the glycosidic torsion from *anti* to high-*anti* region.[50,64] The "ladder-like" transition is an irreversible process, which occurs for reverse K-turns on 10 ns time scales in *ff*94, *ff*99, and *ff*99bsc0 force fields (see Figure 7). The "toxicity" of artificial "ladder-like" rearrangement is similar to α/γ flips that were found to systematically degrade DNA simulations in *ff*94 and *ff*99 force fields.[63] However, the formation of "ladder-like" structures in RNA simulations is apparent on longer time scales, which might be the reason why the A-RNA "ladder-like" artifact has been identified almost three years after the "γ-trans" flips degradation of B-DNA.[63] Similar to α/γ flips in DNA, the "ladder-like" structure is ultimately more stable than the native A-RNA form. The transition is a textbook example of structures where the force field (without the appropriate χ reparameterization) does not provide the correct global minimum of the simulated molecule (or its part), which then sooner or later (depending on the barrier) degrades.[44,63,92,93] This degradation is entirely eliminated in simulations applying the modified χ profiles, i.e., in *ff*99χ_{OL} and *ff*99bsc0χ_{OL} force fields.[64]

It is possible (and not unlikely) that a simple force field with simple analytic function and a limited set of parameters provides a less complex (less flexible) description of structure/energy relations compared to real molecules. Then, refining the force field to reproduce the native conformations may somewhat bias sampling of less populated but still relevant regions of the conformational space. However, at the same time, any force field which has a major pathology is likely not better in sampling of less populated relevant regions. It is because it shares the same function and most parameters with the refined force field but is biased to sample completely unrealistic states as global minima. Therefore, removal of a substantial pathology as done by χ_{OL} should not be accompanied with any systematic bias of less populated nonpathological regions. In addition, the force field has not been primarily fitted to come closer to the native geometry but to reproduce reference QM data. The improvement of the simulation behavior has been achieved indirectly as a

byproduct of the genuine QM fit. The issue of biasing dynamics of less populated relevant states may be, however, a substantial concern when attempting further more subtle changes, i.e., when trying to achieve a perfect reproduction of target structures that would go beyond the principal accuracy limits of a given force field form.

Only trajectories and trajectory portions lacking any sign of the "ladder-like" structure (4.3 μs) are used to assess the dynamics of the reverse K-turns presented here. For these trajectory portions, all solute force fields provide very similar results.

The Effect of Ion and Water Treatment. Compared to the large effect of the RNA force field, the results are considerably less affected by the treatment of the ions and water. However, unkinking of the reverse K-turns is more pronounced in TIP3P in comparison with SPC/E simulations. In contrast, the type and concentration of ions do not appear to substantially affect the reverse K-turn simulations. Consistently with the present results, our earlier reference simulations of A-RNA duplexes comparing the net-neutralizing Na^+ ion ($c(Na^+) \sim 0.2$ M) conditions with the TIP3P water model and KCl excess-salt ($c(K^+) \sim 0.4$ M)) with the SPC/E water model revealed that in SPC/E salt excess the A-RNA structures were more compact, especially for some sequences.[59] Considering the present results, we suggest that the earlier reported differences in A-RNA simulations[59] were caused primarily by the water models rather than by the ionic strength or choice of counterions. Our preliminary data from additional extended MD simulations of A-RNA duplexes under various ionic strengths (data not shown) and solvent models confirm that and will be published elsewhere once completed. Thus, when the simulation conditions are ordered according to their impact on the simulated RNA structures, it appears that the most pronounced effect has the RNA force field. Considerably smaller differences are caused by the used explicit water model (the same applies also for proteins, see refs 84 and 94). Finally, the type and concentration of ions appear to be, so far, less important. This supports the view that most RNA simulations under net-neutralizing conditions are valid, of course provided that the periodic water box size is not too large to dilute the net-neutralizing ions. Further investigations of these issues are under way. It is to be noted that the above considerations are relevant for simulations executed at the presently affordable simulation time scales and with the usual box sizes used in contemporary simulations.

Reverse K-Turns Belong to the Most Flexible Nucleic Acids Molecules Simulated So Far. The X-ray structures of revKt-P9/9.0 and revKt-54 significantly differ (Figures 1 and 6); however, when removed from their structural contexts, both reverse K-turns sample similar structural substates, albeit the sampling at the present simulation time scale is still inevitably affected by the starting structures. Both reverse K-turns sample a wide variety of conformations ranging from fully kinked to fully unkinked states. We observe three types of conformational clusters (substates): (i) the compact fully kinked conformation, (ii) the fully unkinked state, and (iii) the highly flexible intermediate states that reveal hinge-like flexibility correlated with bulge region local dynamics (Figures 6 and 8). While the ribosome utilizes the revKt-54 within its structural context in a geometry corresponding to the flexible intermediate substate, the intron reverse K-turn is locked in the compact fully kinked state.

The fact that reverse K-turns are able to rearrange from fully kinked to fully unkinked substates and vice versa within a relatively short time scale of hundreds of nanoseconds indicates that these motifs are intrinsically metastable in their native conformations and that the barriers between their substates are relatively low (lower than ~7 kcal/mol, which represents the critical free energy barrier for an observable event on the 100 ns time scale). The reverse K-turn is the most flexible recurrent RNA motif studied by MD simulations until now.

Comparison of Simulation Dynamics of K-Turns and Reverse K-Turns. To date, no spontaneous unfolding of conventional K-turns has been observed on tens of nanoseconds time scales of MD simulations.[18,19] When starting from the native folded (tightly kinked) K-turn structures, the simulations reveal hinge-like fluctuations around the native structure similar to what was observed for the intermediate substates of the reverse K-turns. On the other hand, the experimental studies show that the conventional K-turns unfold (unkink) in the absence of proteins or stabilizing divalent cations.[13] Also, the recent NMR structure reveals an extended shape of an isolated K-turn.[95] In contrast to MD simulations, these experimental techniques observe conventional K-turns on much longer time scales and in thermodynamic equilibrium. Unfortunately, experimental data assessing the stability of free reverse K-turns in solution are not currently available. However, taking into account the reverse K-turn simulation data together with the current experimental as well as theoretical knowledge about the stability of conventional K-turns, we can expect that both conventional K-turns and reverse K-turns are most likely able to sample kinked and unkinked substates. The substates of conventional K-turns, however, are separated by higher free energy barriers in comparison to the reverse K-turns. In fact, taking into account the sequence similarity between K-turns and reverse K-turns, we assume that they could both prefer similar unkinked geometries in solution. We expect that both systems could in principle spontaneously attempt transitions between conventional and reverse K-turn bending, albeit this would require unstacking, flipping over, and restacking of terminal NC-stem adenine belonging to the shorter strand (see below), which is most likely a much slower process than the local dynamics of reverse and conventional K-turns.

What Might Be the Role of Reverse K-Turns? We have suggested in earlier studies that, besides their role in protein−RNA interactions, some K-turns can act as flexible molecular elbows involved in functional RNA dynamics during the elongation cycle.[17,19,20] A sufficiently long lifetime of the kinked and unkinked states (originating in the relatively high free energy barrier between both conformational states) can be important for the molecular elbow function of the K-turns, which would utilize the conformational spaces of the kinked state. In contrast, the present simulations show that the reverse K-turns are even more flexible than the conventional K-turns, with a negligible barrier between kinked and unkinked states. Their exact structure is considerably less strictly defined due to the lack of tertiary interstem interactions. Owing to this, the reverse K-turn is also much more versatile in its folded structure (disregarding its context, i.e., intrinsically). We do not have any evidence to suggest that the pronounced elbow-like flexibility of reverse K-turns contributes to large-scale RNA dynamics. Rather, the large flexibility of the reverse K-turns is utilized in RNA folding to build up static RNA 3D topologies based on RNA−RNA interactions. In contrast to conventional K-turns, reverse K-turns do not seem to interact with proteins. This again may be related to the fact that when kinked into reverse K-turn topology, the RNA molecule is still too versatile (less structured) compared to the conventional K-turn topology, due to the lack of tertiary interstem interactions.

Is There a Salient Tertiary Interaction in the Ribosome Responsible for the Reverse K-Turn Bending? The biochemical experiments for the intron revKt-P9/9.0 revealed that a remote tertiary contact is responsible for revKt-P9/9.0 bending.[29] The tertiary contact is formed between the GNRA tetraloop attached to the revKt-P9/9.0 C-stem and receptor atoms situated in the P5/5a intron part (TL-TLR contact). A part of the revKt-54 NC-stem also forms a tertiary interaction, specifically with the minor groove of helix 52. The RNA−RNA interaction does not resemble the intron TL-TLR interface and seems to be a new, as yet unclassified RNA motif or interaction pattern, since the nucleotides as well as the overall 3D topology of this motif are evolutionarily conserved in the ribosome (Figures 4A−D). Furthermore, we have identified an isosteric arrangement in the *glmS* riboswitch.[51,96,97] This motif (see Figure 4E) is the oblique stack interaction between stacked purines (four adenines in the ribosome or the AAGA stack in the *glmS* riboswitch) and the minor groove of the A-RNA stem. In *glmS* riboswitch, this motif includes the P2.1 stem and purine stacking module between P4 and P4.1 stems. It represents a very rigid motif in MD simulations and stabilizes conformation of the pseudoknot carrying the ligand binding site.[51]

We suggest that such an RNA motif stabilizes the kinked conformation of revKt-54 similarly to the intron TL-TLR interface. These interactions, which are localized in outer parts of the reverse K-turns, are most likely responsible for the bending of reverse K-turns, because without this tertiary RNA−RNA interaction both reverse K-turns easily relax to more extended structures. As the bending is imposed by external interactions with respect to the reverse K-turns, there is no direct evolutionary pressure for reverse K-turns' primary sequence conservation around the bulge. Other RNA sequences with appropriate bending capability could replace the reverse K-turn. This actually happens in the course of evolution since our simulations show that the revKt-54 structural analog from *E.c.*, which has a very different sequence in comparison to revKt-54, exhibits the same flexibility (see the Supporting Information). This strikingly resembles the evolutionary variability of the elbow segment at the base of the dynamical A-site finger of the large ribosomal subunit.[17] Also, in that case, a structured RNA motif in *H.m.* is, in bacteria, replaced by at first sight unrelated RNA segments which nevertheless adopt an identical global topology and have strikingly similar simulation behavior. Thus, evolution is capable of replacing one RNA element with another one, which looks unrelated at the level of sequence, 2D structure, as well as molecular interactions but still conserves key physical-chemistry properties (such as topology and directional flexibility) required for proper function.[17,98] These observations illustrate the modular nature of large RNA molecules, where distinct medium-sized recurrent RNA molecular building blocks are used to create large functional RNA structures. Computations can in such cases provide useful insights complementing the structural and bioinformatics data.

Why Is the First *t*HS G/A Base Pair of the NC-Stem of K-Turn Replaced by the *t*HH A/A Base Pair in Reverse K-Turn? The only significant sequence difference between K-turn and reverse K-turn structures is the (first, terminal) base pair of the NC-stem adjacent to the bulge. This base pair is critical for the bending direction, which is driven by the bend of the shorter strand, while the longer "bulge" strand passively follows (Figure 9 and Figure S14, Supporting Information). In conventional K-turns, the terminal base pair of the NC-stem must have adenine in the short strand and must be a *t*HS base pair.[30] It is due to its

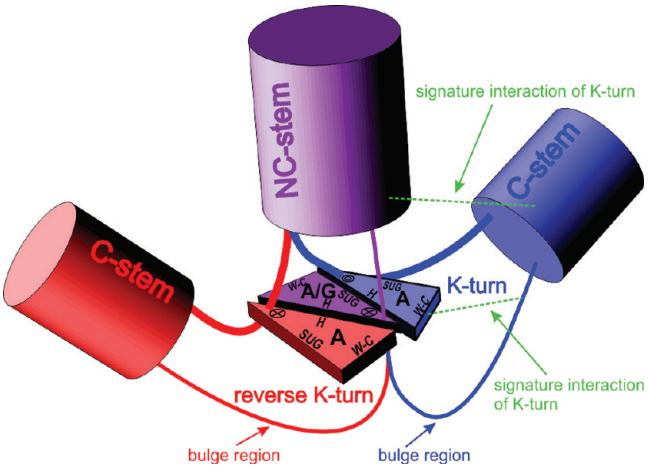

Figure 9. Scheme of the role of the flipped-over adenine (red) in reverse K-turn and the corresponding opposite bending of the K-turn (blue) and reverse K-turn (red). Both systems are superimposed over their NC-stems (the shared parts are in violet). The thick and thin lines highlight the short and long strands, respectively. The terminal base pair of NC-stem adjacent to the bulge is represented in a triangle abstraction.[102] Note that the red and blue triangles are flipped-over with respect to each other, so that they stack on the NC-stem by different nucleobase faces. The green dashed line shows the signature interactions of K-turn. The Supporting Information presents an analogical superposition of reverse K-turn revKt-54 and consensual K-turn Kt-7 structures over their NC-stem backbone atoms (Figure S14, Supporting Information).

adenine-specific N1 acceptor signature interaction with the bulge 5′-most nucleotide which firmly stacks on the C-stem.[1,30] Once this interaction is formed, only the Hoogsteen-edge of the short-strand adenine remains available (Figure S15A, Supporting Information). The first NC-stem base pair is then completed by a nucleotide from the longer strand to adopt the *t*HS arrangement (see Supporting Information for further details). The *t*HS arrangement is needed to insert the immediately following longer-strand adenine (belonging to the second base pair in the NC-stem) through its sugar edge to the minor groove of the C-stem to form the A-minor interaction between the NC- and C-stems (Figure S15B, Supporting Information). This finally fixes the overall K-turn topology (Figure S15C, Supporting Information). Among the *t*HS base pairs, the A/G base pair is energetically the most stable[99] and the most frequently realized in the naturally occurring RNAs.[100] The isosteric *t*HS A/A base pair would also be geometrically entirely compatible with the topology of conventional the K-turn but is energetically less stable[99] and also less frequent in RNAs.[100] Sequence alignments reveal that the A/A combination indeed is sometimes realized in K-turns.[14,30]

In contrast, the *t*HS base pair is incompatible with the topology of reverse K-turns. Similarly to conventional K-turns, the first nucleotide of the shorter strand in NC-stem is adenine and offers only its Hoogsteen-edge for pairing (Figure S14, Supporting Information). However, this adenine is flipped over and stacked to the NC-stem by the opposite stacking face in comparison with K-turn (and stacking in A-form RNA). Then, the shorter strand is bent in the opposite direction to that in K-turn motif (Figure 9). This rearrangement of shorter strand flips its terminal adenine of NC-stem toward the Hoogsteen-edge of the second nucleotide in the corresponding base pair, and thus the terminal base pair of NC-stem is paired in a *t*HH manner

in reverse K-turn (Figure 9). Such flip reverting strand direction was also observed in the S-turn motif of the sarcin−ricin loop, where two consequent flips form the S-shaped appearance of this motif.[101] Similarly to the sarcin−ricin loop, the flipped over adenine offers its 2′-hydroxyl group to the major groove of NC-stem forming a sugar−phosphate interaction with the *pro*-R_P nonbridging oxygen of its upstream nucleotide, in contrast to A-RNA where 2′-hydroxyl groups are exposed to the minor groove. The A/A is the most frequent *t*HH base pair in known RNAs,[100] since it is supported by the adenine-specific base−phosphate interaction. The *t*HH A/G base pair is basically absent in natural RNAs, as it does not offer a favorable combination of donors and acceptors. Thus, the difference in topology between reverse and conventional K-turns together with energetics of molecular interactions dictate the replacement of the *t*HS A/G K-turn combination with the *t*HH A/A reverse K-turn combination. While the *t*HS A/G base pair can covary with A/A, the covariation of the *t*HH A/A base pair with A/G is less likely. Despite this, the X-ray structure of the A201G mutant shows that the *t*HH A/G can be stable within the structural context of reverse K-turn within the group I intron.[29] Such covariation, however, is not expected in naturally occurring sequences.[100] Overall, the conservation of the *t*HH A/A base pair terminating the NC-stem with flipped over adenine is rather a consequence of evolutionarily conserved outlaying tertiary RNA−RNA interactions determining the direction of the reverse K-turn bend. More detailed explanation can be found in the Supporting Information.

■ ASSOCIATED CONTENT

Supporting Information. Definition of substates; mathematical definition of interhelical angle dihedral followed by a discussion of their limitations; extended discussion about the conservation of *t*HS A/G and *t*HH A/A base pairs in conventional and reverse K-turns, respectively. Figures S1−S15 and Tables S1−S5 giving the supplemental RMSD vs R_g plots; scheme of end-to-end distance, interhelical angle, and dihedral; plot of these parameters for reverse K-turns' substates; secondary and 3D structures of eubacterial revKt-54-analogs; secondary structure of *E.c.* revKt-54-analog; RNA−RNA tertiary interactions of eubacterial revKt-54-analogs; "ladder-like" conformations of both reverse K-turns; representative structures of both reverse K-turns' substates; density maps of Na^+ and K^+ around revKt-P9/9.0; NC-stem superposition of revKt-54 with the consensual K-turn Kt-7; signature interactions in K-turn Kt-7; list of RMSD and R_g intervals utilized for definition of substates; values of interhelical angles, interhelical dihedrals, and end-to-end distances for reverse K-turns' crystal structures and their substates from MD simulations; list of additional simulations; contribution of the first five essential dynamics modes in intermediate substates; absolute and relative free energies of revKt-P9/9.0 and revKt-54 substates calculated by the MM-PBSA method. This material is available free of charge via the Internet at http://pubs.acs.org.

■ AUTHOR INFORMATION

Corresponding Authors

*Tel: +420 585 634 756 (M.O.), +420 541 517 133 (J.S.). Fax: +420 585 634 761 (M.O.). E-mail: michal.otyepka@upol.cz, sponer@ncbr.chemi.muni.cz.

■ ACKNOWLEDGMENT

This work was supported by the Grant Agency of the Academy of Sciences of the Czech Republic (grants KJB400040901 and IAA400040802), by the Grant Agency of the Czech Republic (grants 203/09/H046, 203/09/1476, P208/11/1822, and P301/11/P558), by Ministry of Youth, Sport and Education of Czech Republic (grants CZ.1.05/2.1.00/03.0058, CZ.1.07/2.3.00/20.0017, LC06030, LC512, and MSM6198959216), by Student Project PrF_2011_020 of Palacky University, and by the Academy of Sciences of the Czech Republic (grants no. AV0Z50040507, AV0Z50040702, and Z40550506). F.L. gratefully acknowledges the support of the J.E. Purkyne Fellowship from the Academy of Sciences of the Czech Republic.

■ REFERENCES

(1) Klein, D. J.; Schmeing, T. M.; Moore, P. B.; Steitz, T. A. The kink-turn: a new RNA secondary structure motif. *EMBO J.* **2001**, *20*, 4214–4221.

(2) Schuwirth, B. S.; Borovinskaya, M. A.; Hau, C. W.; Zhang, W.; Vila-Sanjurjo, A.; Holton, J. M.; Cate, J. H. Structures of the bacterial ribosome at 3.5 A resolution. *Science* **2005**, *310*, 827–834.

(3) Wimberly, B. T.; Brodersen, D. E.; Clemons, W. M., Jr.; Morgan-Warren, R. J.; Carter, A. P.; Vonrhein, C.; Hartsch, T.; Ramakrishnan, V. Structure of the 30S ribosomal subunit. *Nature* **2000**, *407*, 327–339.

(4) Mao, H.; White, S. A.; Williamson, J. R. A novel loop-loop recognition motif in the yeast ribosomal protein L30 autoregulatory RNA complex. *Nat. Struct. Biol.* **1999**, *6*, 1139–1147.

(5) White, S. A.; Hoeger, M.; Schweppe, J. J.; Shillingford, A.; Shipilov, V.; Zarutskie, J. Internal loop mutations in the ribosomal protein L30 binding site of the yeast L30 RNA transcript. *RNA* **2004**, *10*, 369–377.

(6) Montange, R. K.; Batey, R. T. Structure of the S-adenosylmethionine riboswitch regulatory mRNA element. *Nature* **2006**, *441*, 1172–1175.

(7) Blouin, S.; Lafontaine, D. A. A loop loop interaction and a K-turn motif located in the lysine aptamer domain are important for the riboswitch gene regulation control. *RNA* **2007**, *13*, 1256–1267.

(8) Watkins, N. J.; Segault, V.; Charpentier, B.; Nottrott, S.; Fabrizio, P.; Bachi, A.; Wilm, M.; Rosbash, M.; Branlant, C.; Luhrmann, R. A common core RNP structure shared between the small nucleoar box C/D RNPs and the spliceosomal U4 snRNP. *Cell* **2000**, *103*, 457–466.

(9) Vidovic, I.; Nottrott, S.; Hartmuth, K.; Luhrmann, R.; Ficner, R. Crystal structure of the spliceosomal 15.5kD protein bound to a U4 snRNA fragment. *Mol. Cell* **2000**, *6*, 1331–1342.

(10) Wozniak, A. K.; Nottrott, S.; Kuhn-Holsken, E.; Schroder, G. F.; Grubmuller, H.; Luhrmann, R.; Seidel, C. A.; Oesterhelt, F. Detecting protein-induced folding of the U4 snRNA kink-turn by single-molecule multiparameter FRET measurements. *RNA* **2005**, *11*, 1545–1554.

(11) Yusupov, M. M.; Yusupova, G. Z.; Baucom, A.; Lieberman, K.; Earnest, T. N.; Cate, J. H. D.; Noller, H. F. Crystal structure of the ribosome at 5.5 angstrom resolution. *Science* **2001**, *292*, 883–896.

(12) Turner, B.; Melcher, S. E.; Wilson, T. J.; Norman, D. G.; Lilley, D. M. Induced fit of RNA on binding the L7Ae protein to the kink-turn motif. *RNA* **2005**, *11*, 1192–1200.

(13) Goody, T. A.; Melcher, S. E.; Norman, D. G.; Lilley, D. M. The kink-turn motif in RNA is dimorphic, and metal ion-dependent. *RNA* **2004**, *10*, 254–264.

(14) Schroeder, K. T.; McPhee, S. A.; Ouellet, J.; Lilley, D. M. A structural database for k-turn motifs in RNA. *RNA* **2010**, *16*, 1463–1468.

(15) Schroeder, K. T.; Lilley, D. M. Ion-induced folding of a kink turn that departs from the conventional sequence. *Nucleic Acids Res.* **2009**, *37*, 7281–7289.

(16) Spackova, N.; Reblova, K.; Sponer, J. Structural dynamics of the box C/D RNA kink-turn and its complex with proteins: the role of the A-minor 0 interaction, long-residency water bridges, and structural

ion-binding sites revealed by molecular simulations. *J. Phys. Chem. B* **2010**, *114*, 10581–10593.

(17) Reblova, K.; Razga, F.; Li, W.; Gao, H.; Frank, J.; Sponer, J. Dynamics of the base of ribosomal A-site finger revealed by molecular dynamics simulations and Cryo-EM. *Nucleic Acids Res.* **2010**, *38*, 1325–1340.

(18) Razga, F.; Koca, J.; Mokdad, A.; Sponer, J. Elastic properties of ribosomal RNA building blocks: molecular dynamics of the GTPase-associated center rRNA. *Nucleic Acids Res.* **2007**, *35*, 4007–4017.

(19) Razga, F.; Zacharias, M.; Reblova, K.; Koca, J.; Sponer, J. RNA kink-turns as molecular elbows: hydration, cation binding, and large-scale dynamics. *Structure* **2006**, *14*, 825–835.

(20) Razga, F.; Koca, J.; Sponer, J.; Leontis, N. B. Hinge-like motions in RNA kink-turns: the role of the second a-minor motif and nominally unpaired bases. *Biophys. J.* **2005**, *88*, 3466–3485.

(21) Razga, F.; Spackova, N.; Reblova, K.; Koca, J.; Leontis, N. B.; Sponer, J. Ribosomal RNA kink-turn motif--a flexible molecular hinge. *J. Biomol. Struct. Dyn.* **2004**, *22*, 183–194.

(22) Curuksu, J.; Sponer, J.; Zacharias, M. Elbow flexibility of the kt38 RNA kink-turn motif investigated by free-energy molecular dynamics simulations. *Biophys. J.* **2009**, *97*, 2004–2013.

(23) Leontis, N. B.; Stombaugh, J.; Westhof, E. The non-Watson-Crick base pairs and their associated isostericity matrices. *Nucleic Acids Res.* **2002**, *30*, 3497–3531.

(24) Sarver, M.; Zirbel, C. L.; Stombaugh, J.; Mokdad, A.; Leontis, N. B. FR3D: finding local and composite recurrent structural motifs in RNA 3D structures. *J. Math. Biol.* **2008**, *56*, 215–252.

(25) Liu, J.; Lilley, D. M. The role of specific 2′-hydroxyl groups in the stabilization of the folded conformation of kink-turn RNA. *RNA* **2007**, *13*, 200–210.

(26) Szewczak, L. B.; Gabrielsen, J. S.; Degregorio, S. J.; Strobel, S. A.; Steitz, J. A. Molecular basis for RNA kink-turn recognition by the h15.5K small RNP protein. *RNA* **2005**, *11*, 1407–1419.

(27) Nissen, P.; Ippolito, J. A.; Ban, N.; Moore, P. B.; Steitz, T. A. RNA tertiary interactions in the large ribosomal subunit: the A-minor motif. *Proc. Natl. Acad. Sci. U. S. A.* **2001**, *98*, 4899–4903.

(28) Adams, P. L.; Stahley, M. R.; Kosek, A. B.; Wang, J.; Strobel, S. A. Crystal structure of a self-splicing group I intron with both exons. *Nature* **2004**, *430*, 45–50.

(29) Antonioli, A. H.; Cochrane, J. C.; Lipchock, S. V.; Strobel, S. A. Plasticity of the RNA kink turn structural motif. *RNA* **2010**, *16*, 762–768.

(30) Leontis, N. B.; Lescoute, A.; Westhof, E. The building blocks and motifs of RNA architecture. *Curr. Opin. Struct. Biol.* **2006**, *16*, 279–287.

(31) Strobel, S. A.; Adams, P. L.; Stahley, M. R.; Wang, J. RNA kink turns to the left and to the right. *RNA* **2004**, *10*, 1852–1854.

(32) Klein, D. J.; Moore, P. B.; Steitz, T. A. The roles of ribosomal proteins in the structure assembly, and evolution of the large ribosomal subunit. *J. Mol. Biol.* **2004**, *340*, 141–177.

(33) Blaha, G.; Gurel, G.; Schroeder, S. J.; Moore, P. B.; Steitz, T. A. Mutations outside the anisomycin-binding site can make ribosomes drug-resistant. *J. Mol. Biol.* **2008**, *379*, 505–519.

(34) Zhong, C.; Tang, H.; Zhang, S. RNAMotifScan: automatic identification of RNA structural motifs using secondary structural alignment. *Nucleic Acids Res.* **2010**, *38*, e176.

(35) Xin, Y.; Hamelberg, D. Deciphering the role of glucosamine-6-phosphate in the riboswitch action of glmS ribozyme. *RNA* **2010**, *16*, 2455–2463.

(36) Fulle, S.; Christ, N. A.; Kestner, E.; Gohlke, H. HIV-1 TAR RNA spontaneously undergoes relevant apo-to-holo conformational transitions in molecular dynamics and constrained geometrical simulations. *J. Chem. Inf. Model.* **2010**, *50*, 1489–1501.

(37) Fulle, S.; Gohlke, H. Molecular recognition of RNA: challenges for modelling interactions and plasticity. *J. Mol. Recognit.* **2010**, *23*, 220–231.

(38) Freedman, H.; Huynh, L. P.; Le, L.; Cheatham, T. E., 3rd; Tuszynski, J. A.; Truong, T. N. Explicitly solvated ligand contribution to continuum solvation models for binding free energies: selectivity of theophylline binding to an RNA aptamer. *J. Phys. Chem. B* **2010**, *114*, 2227–2237.

(39) Huang, W.; Kim, J.; Jha, S.; Aboul-ela, F. A mechanism for S-adenosyl methionine assisted formation of a riboswitch conformation: a small molecule with a strong arm. *Nucleic Acids Res.* **2009**, *37*, 6528–6539.

(40) Orozco, M.; Noy, A.; Perez, A. Recent advances in the study of nucleic acid flexibility by molecular dynamics. *Curr. Opin. Struct. Biol.* **2008**, *18*, 185–193.

(41) McCrate, N. E.; Varner, M. E.; Kim, K. I.; Nagan, M. C. Molecular dynamics simulations of human tRNA Lys,3 UUU: the role of modified bases in mRNA recognition. *Nucleic Acids Res.* **2006**, *34*, 5361–5368.

(42) Cheatham, T. E., 3rd. Simulation and modeling of nucleic acid structure, dynamics and interactions. *Curr. Opin. Struct. Biol.* **2004**, *14*, 360–367.

(43) Hall, K. B. RNA in motion. *Curr. Opin. Chem. Biol.* **2008**, *12*, 612–618.

(44) Ditzler, M. A.; Otyepka, M.; Sponer, J.; Walter, N. G. Molecular dynamics and quantum mechanics of RNA: conformational and chemical change we can believe. *Acc. Chem. Res.* **2010**, *43*, 40–47.

(45) Reblova, K.; Spackova, N.; Stefl, R.; Csaszar, K.; Koca, J.; Leontis, N. B.; Sponer, J. Non-Watson-Crick basepairing and hydration in RNA motifs: molecular dynamics of 5S rRNA loop E. *Biophys. J.* **2003**, *84*, 3564–3582.

(46) Spackova, N.; Sponer, J. Molecular dynamics simulations of sarcin-ricin rRNA motif. *Nucleic Acids Res.* **2006**, *34*, 697–708.

(47) Romanowska, J.; Setny, P.; Trylska, J. Molecular dynamics study of the ribosomal A-site. *J. Phys. Chem. B* **2008**, *112*, 15227–15243.

(48) Veeraraghavan, N.; Ganguly, A.; Chen, J. H.; Bevilacqua, P. C.; Hammes-Schiffer, S.; Golden, B. L. Metal Binding Motif in the Active Site of the HDV Ribozyme Binds Divalent and Monovalent Ions. *Biochemistry* **2011**, *50*, 2672–2682.

(49) Krasovska, M. V.; Sefcikova, J.; Reblova, K.; Schneider, B.; Walter, N. G.; Sponer, J. Cations and hydration in catalytic RNA: molecular dynamics of the hepatitis delta virus ribozyme. *Biophys. J.* **2006**, *91*, 626–638.

(50) Mlynsky, V.; Banas, P.; Hollas, D.; Reblova, K.; Walter, N. G.; Sponer, J.; Otyepka, M. Extensive molecular dynamics simulations showing that canonical G8 and protonated A38H+ forms are most consistent with crystal structures of hairpin ribozyme. *J. Phys. Chem. B* **2010**, *114*, 6642–6652.

(51) Banas, P.; Walter, N. G.; Sponer, J.; Otyepka, M. Protonation states of the key active site residues and structural dynamics of the glmS riboswitch as revealed by molecular dynamics. *J. Phys. Chem. B* **2010**, *114*, 8701–8712.

(52) Villa, A.; Wohnert, J.; Stock, G. Molecular dynamics simulation study of the binding of purine bases to the aptamer domain of the guanine sensing riboswitch. *Nucleic Acids Res.* **2009**, *37*, 4774–4786.

(53) Reblova, K.; Fadrna, E.; Sarzynska, J.; Kulinski, T.; Kulhanek, P.; Ennifar, E.; Koca, J.; Sponer, J. Conformations of flanking bases in HIV-1 RNA DIS kissing complexes studied by molecular dynamics. *Biophys. J.* **2007**, *93*, 3932–3949.

(54) Bahadur, R. P.; Kannan, S.; Zacharias, M. Binding of the bacteriophage P22 N-peptide to the boxB RNA motif studied by molecular dynamics simulations. *Biophys. J.* **2009**, *97*, 3139–3149.

(55) Reblova, K.; Lankas, F.; Razga, F.; Krasovska, M. V.; Koca, J.; Sponer, J. Structure, dynamics, and elasticity of free 16s rRNA helix 44 studied by molecular dynamics simulations. *Biopolymers* **2006**, *82*, 504–520.

(56) Besseova, I.; Reblova, K.; Leontis, N. B.; Sponer, J. Molecular dynamics simulations suggest that RNA three-way junctions can act as flexible RNA structural elements in the ribosome. *Nucleic Acids Res.* **2010**, *38*, 6247–6264.

(57) Shankar, N.; Kennedy, S. D.; Chen, G.; Krugh, T. R.; Turner, D. H. The NMR structure of an internal loop from 23S ribosomal RNA differs from its structure in crystals of 50s ribosomal subunits. *Biochemistry* **2006**, *45*, 11776–11789.

(58) Reblova, K.; Strelcova, Z.; Kulhanek, P.; Besscova, I.; Mathews, D. H.; Van Nostrand, K.; Yildirim, I.; Turner, D. H.; Sponer, J. An RNA Molecular Switch: Intrinsic Flexibility of 23S rRNA Helices 40 and 68 5′-UAA/5′-GAN Internal Loops Studied by Molecular Dynamics Methods. *J. Chem. Theory Comput.* **2010**, *6*, 910–929.

(59) Besseova, I.; Otyepka, M.; Reblova, K.; Sponer, J. Dependence of A-RNA simulations on the choice of the force field and salt strength. *Phys. Chem. Chem. Phys.* **2009**, *11*, 10701–10711.

(60) Pearlman, D. A.; Case, D. A.; Caldwell, J. W.; Ross, W. S.; Cheatham, T. E.; Debolt, S.; Ferguson, D.; Seibel, G.; Kollman, P. Amber, a Package of Computer-Programs for Applying Molecular Mechanics, Normal-Mode Analysis, Molecular-Dynamics and Free-Energy Calculations to Simulate the Structural and Energetic Properties of Molecules. *Comput. Phys. Commun.* **1995**, *91*, 1–41.

(61) Cornell, W. D.; Cieplak, P.; Bayly, C. I.; Gould, I. R.; Merz, K. M.; Ferguson, D. M.; Spellmeyer, D. C.; Fox, T.; Caldwell, J. W.; Kollman, P. A. A 2nd. Generation Force-Field for the Simulation of Proteins Nucleic-Acids, and Organic-Molecules. *J. Am. Chem. Soc.* **1995**, *117*, 5179–5197.

(62) Wang, J. M.; Cieplak, P.; Kollman, P. A. How well does a restrained electrostatic potential (RESP) model perform in calculating conformational energies of organic and biological molecules? *J. Comput. Chem.* **2000**, *21*, 1049–1074.

(63) Perez, A.; Marchan, I.; Svozil, D.; Sponer, J.; Cheatham, T. E., 3rd; Laughton, C. A.; Orozco, M. Refinement of the AMBER force field for nucleic acids: improving the description of alpha/gamma conformers. *Biophys. J.* **2007**, *92*, 3817–3829.

(64) Banas, P.; Hollas, D.; Zgarbova, M.; Jurecka, P.; Orozco, M.; Cheatham, T. E.; Sponer, J.; Otyepka, M. Performance of Molecular Mechanics Force Fields for RNA Simulations: Stability of UUCG and GNRA Hairpins. *J. Chem. Theory Comput.* **2010**, *6*, 3836–3849.

(65) Aqvist, J. Ion Water Interaction Potentials Derived from Free-Energy Perturbation Simulations. *J. Phys. Chem.* **1990**, *94*, 8021–8024.

(66) Jorgensen, W. L.; Chandrasekhar, J.; Madura, J. D.; Impey, R. W.; Klein, M. L. Comparison of Simple Potential Functions for Simulating Liquid Water. *J. Chem. Phys.* **1983**, *79*, 926–935.

(67) Dang, L. X.; Kollman, P. A. Free-Energy of Association of the K +18-Crown-6 Complex in Water - a New Molecular-Dynamics Study. *J. Phys. Chem.* **1995**, *99*, 55–58.

(68) Smith, D. E.; Dang, L. X. Computer-Simulations of Nacl Association in Polarizable Water. *J. Chem. Phys.* **1994**, *100*, 3757–3766.

(69) Berendsen, H. J. C.; Grigera, J. R.; Straatsma, T. P. The Missing Term in Effective Pair Potentials. *J. Phys. Chem.* **1987**, *91*, 6269–6271.

(70) Joung, I. S.; Cheatham, T. E., 3rd. Determination of alkali and halide monovalent ion parameters for use in explicitly solvated biomolecular simulations. *J. Phys. Chem. B* **2008**, *112*, 9020–9041.

(71) Noy, A.; Soteras, I.; Luque, F. J.; Orozco, M. The impact of monovalent ion force field model in nucleic acids simulations. *Phys. Chem. Chem. Phys.* **2009**, *11*, 10596–10607.

(72) Darden, T.; York, D.; Pedersen, L. Particle Mesh Ewald - an N. Log(N) Method for Ewald Sums in Large Systems. *J. Chem. Phys.* **1993**, *98*, 10089–10092.

(73) Essmann, U.; Perera, L.; Berkowitz, M. L.; Darden, T.; Lee, H.; Pedersen, L. G. A Smooth Particle Mesh Ewald Method. *J. Chem. Phys.* **1995**, *103*, 8577–8593.

(74) DeLano, W. L. *The PyMOL Molecular Graphics System*; DeLano Scientific LLC: Palo Alto, CA, 2008.

(75) Humphrey, W.; Dalke, A.; Schulten, K. VMD: Visual molecular dynamics. *J. Mol. Graphics* **1996**, *14*, 33–38.

(76) Lankas, F.; Spackova, N.; Moakher, M.; Enkhbayar, P.; Sponer, J. A measure of bending in nucleic acids structures applied to A-tract DNA. *Nucleic Acids Res.* **2010**, *38*, 3414–3422.

(77) Case, D. A.; Darden, T. A.; Cheatham, T. E., 3rd; Simmerling, C. L.; Wang, J.; Duke, R. E.; Luo, R.; Walker, R. C.; Zhang, W.; Merz, K. M.; Roberts, B.; Wang, B.; Hayik, S.; Roitberg, A.; Seabra, G.; Kolossváry, I.; Wong, K. F.; Paesani, F.; Vanicek, J.; Liu, J.; Wu, X.; Brozell, S. R.; Steinbrecher, T.; Gohlke, H.; Cai, Q.; Ye, X.; Wang, J.; Hsieh, M.-J.; Cui, G.; Roe, D. R.; Mathews, D. H.; Seetin, M. G.; Sagui, C.; Babin, V.; Luchko, T.; Gusarov, S.; Kovalenko, A.; Kollman, P. A. *AMBER 11*; University of California: San Francisco, CA, 2010.

(78) Luo, R.; David, L.; Gilson, M. K. Accelerated Poisson-Boltzmann calculations for static and dynamic systems. *J. Comput. Chem.* **2002**, *23*, 1244–1253.

(79) Tsui, V.; Case, D. A. Theory and applications of the generalized Born solvation model in macromolecular simulations. *Biopolymers* **2000**, *56*, 275–291.

(80) Hess, B.; Kutzner, C.; van der Spoel, D.; Lindahl, E. GROMACS 4: Algorithms for highly efficient, load-balanced, and scalable molecular simulation. *J. Chem. Theory Comput.* **2008**, *4*, 435–447.

(81) Zirbel, C. L.; Sponer, J. E.; Sponer, J.; Stombaugh, J.; Leontis, N. B. Classification and energetics of the base-phosphate interactions in RNA. *Nucleic Acids Res.* **2009**, *37*, 4898–4918.

(82) Ennifar, E.; Walter, P.; Dumas, P. A crystallographic study of the binding of 13 metal ions to two related RNA duplexes. *Nucleic Acids Res.* **2003**, *31*, 2671–2682.

(83) Reblova, K.; Spackova, N.; Sponer, J. E.; Koca, J.; Sponer, J. Molecular dynamics simulations of RNA kissing-loop motifs reveal structural dynamics and formation of cation-binding pockets. *Nucleic Acids Res.* **2003**, *31*, 6942–6952.

(84) Florova, P.; Sklenovsky, P.; Banas, P.; Otyepka, M. Explicit Water Models Affect the Specific Solvation and Dynamics of Unfolded Peptides While the Conformational Behavior and Flexibility of Folded Peptides Remain Intact. *J. Chem. Theory Comput.* **2010**, *6*, 3569–3579.

(85) Banas, P.; Jurecka, P.; Walter, N. G.; Sponer, J.; Otyepka, M. Theoretical studies of RNA catalysis: hybrid QM/MM methods and their comparison with MD and QM. *Methods* **2009**, *49*, 202–216.

(86) Sponer, J.; Sabat, M.; Gorb, L.; Leszczynski, J.; Lippert, B.; Hobza, P. The effect of metal binding to the N7 site of purine nucleotides on their structure, energy, and involvement in base pairing. *J. Phys. Chem. B* **2000**, *104*, 7535–7544.

(87) Katz, A. K.; Glusker, J. P.; Beebe, S. A.; Bock, C. W. Calcium ion coordination: A comparison with that of beryllium, magnesium, and zinc. *J. Am. Chem. Soc.* **1996**, *118*, 5752–5763.

(88) Dudev, T.; Lim, C. Metal binding affinity and selectivity in metalloproteins: Insights from computational studies. *Ann. Rev. Biophys.* **2008**, *37*, 97–116.

(89) Petrov, A. S.; Bowman, J. C.; Harvey, S. C.; Williams, L. D. Bidentate RNA-magnesium clamps: on the origin of the special role of magnesium in RNA folding. *RNA* **2011**, *17*, 291–297.

(90) Gresh, N.; Sponer, J. E.; Spackova, N.; Leszczynski, J.; Sponer, J. Theoretical study of binding of hydrated Zn(II) and Mg(II) cations to 5′-guanosine monophosphate. Toward polarizable molecular mechanics for DNA and RNA. *J. Phys. Chem. B* **2003**, *107*, 8669–8681.

(91) Dudev, T.; Lim, C. Principles governing Mg, Ca, and Zn binding and selectivity in proteins. *Chem. Rev.* **2003**, *103*, 773–788.

(92) Fadrna, E.; Spackova, N.; Stefl, R.; Koca, J.; Cheatham, T. E., 3rd; Sponer, J. Molecular dynamics simulations of Guanine quadruplex loops: advances and force field limitations. *Biophys. J.* **2004**, *87*, 227–242.

(93) Fadrna, E.; Spackova, N.; Sarzynska, J.; Koca, J.; Orozco, M.; Cheatham, T. E.; Kulinski, T.; Sponer, J. Single Stranded Loops of Quadruplex DNA As Key Benchmark for Testing Nucleic Acids Force Fields. *J. Chem. Theory Comput.* **2009**, *5*, 2514–2530.

(94) Cerutti, D. S.; Freddolino, P. L.; Duke, R. E., Jr.; Case, D. A. Simulations of a protein crystal with a high resolution X-ray structure: evaluation of force fields and water models. *J. Phys. Chem. B* **2010**, *114*, 12811–12824.

(95) Falb, M.; Amata, I.; Gabel, F.; Simon, B.; Carlomagno, T. Structure of the K-turn U4 RNA: a combined NMR and SANS study. *Nucleic Acids Res.* **2010**, *38*, 6274–6285.

(96) Klein, D. J.; Ferre-D'Amare, A. R. Structural basis of glmS ribozyme activation by glucosamine-6-phosphate. *Science* **2006**, *313*, 1752–1756.

(97) Cochrane, J. C.; Lipchock, S. V.; Strobel, S. A. Structural investigation of the GlmS ribozyme bound to Its catalytic cofactor. *Chem. Biol.* **2007**, *14*, 97–105.

(98) Jaeger, L.; Verzemnieks, E. J.; Geary, C. The UA_handle: a versatile submotif in stable RNA architectures. *Nucleic Acids Res.* **2009**, *37*, 215–230.

(99) Mladek, A.; Sharma, P.; Mitra, A.; Bhattacharyya, D.; Sponer, J.; Sponer, J. E. Trans Hoogsteen/sugar edge base pairing in RNA. Structures, energies, and stabilities from quantum chemical calculations. *J. Phys. Chem. B* **2009**, *113*, 1743–1755.

(100) Stombaugh, J.; Zirbel, C. L.; Westhof, E.; Leontis, N. B. Frequency and isostericity of RNA base pairs. *Nucleic Acids Res.* **2009**, *37*, 2294–2312.

(101) Correll, C. C.; Munishkin, A.; Chan, Y. L.; Ren, Z.; Wool, I. G.; Steitz, T. A. Crystal structure of the ribosomal RNA domain essential for binding elongation factors. *Proc. Natl. Acad. Sci. U. S. A.* **1998**, *95*, 13436–13441.

(102) Leontis, N. B.; Westhof, E. Geometric nomenclature and classification of RNA base pairs. *RNA* **2001**, *7*, 499–512.

(103) Zgarbova, M.; Otyepka, M.; Sponer, J.; Mladek, A.; Banas, P.; Cheatham, T. E.; Jurecka, P. Refinement of the Cornell et al. Nucleic Acids Force Field based on Reference Quantum Chemical Calculations of Glycosidic Torsion Profiles. *J. Chem. Theory Comput.* **2011**, in press (DOI: 10.1021/ct200162x).